W Boson Physics at Hadron Colliders

Randy M. Thurman-Keup

Argonne National Laboratory, Argonne, Illinois 60439

Ashutosh V. Kotwal

Duke University, Durham, North Carolina 27708

Monica Tecchio

University of Michigan, Ann Arbor, Michigan 48109

Aesook Byon-Wagner

Fermi National Accelerator Laboratory, Batavia, Illinois 60510

The use of hadron colliders to investigate the properties of the W bosons started in 1982. Since then, the Tevatron experiments have recorded large sample of W events which resulted in precision measurements of the properties of W bosons. In this paper we review the W gauge boson physics at hadron colliders from 1982 to 2000. We present the production mechanism and detection of W bosons in $p\overline{p}$ collisions. We briefly review the history of early studies and give a through examination of W boson physics at the Tevatron collider. Finally, we discuss the directions of W boson physics at hadron colliders after the year 2000.

CONTENTS

I. INTRODUCTION

The massive charged $W^{\pm}$ and neutral Z^0 bosons were proposed in the 60's as the mediators of the weak currents in the unified model of electromagnetic and weak interactions developed by Glashow (1961), Weinberg (1967), and Salam (1969). This model, now known as the "standard" model, reconciles under a unified theory the pure

V-A nature of the charged weak currents with the predominant V-A nature of neutral weak currents by including the electromagnetic current and imposing local gauge invariance under the $SU(2)_L \times U(1)_Y$ symmetry group. The requirement of local gauge invariance and its "spontaneous" breaking via the Higgs mechanism ensures that the theory remains renormalizable, i.e. it prevents the divergences in the high energy limit that had plagued previous models of the weak currents.

While the phenomenology of the charged weak currents was well established at the time, the neutral weak currents had not been observed yet. Their discovery in $\nu_\mu N \to \nu_\mu X$ scattering at the CERN Gargamelle bubble chamber in 1973 (Hasert *et al.*, 1973) was the first success of the standard model. But its most spectacular confirmation came with the discovery in 1983 of the W and Z bosons by the UA1 and UA2 experiments at the CERN $Sp\overline{p}S$ collider at the masses predicted from neutrino-scattering data and the muon lifetime. The 90's saw increasingly precise experimental tests of the standard model predictions. Studies at the Z resonance by the LEP and SLC detectors tested the theory of weak neutral currents to higher orders in perturbation theory (see Grünewald, 1999 for a recent review). In this paper we will review the direct measurements of the properties of the W boson in charged weak interactions at the Tevatron $p\overline{p}$ collider.

A. Role of the W Boson in Electro-weak Physics

In the standard model (SM), the intermediate vector bosons arise as combinations of the isotriplet of vector fields $W^i_\mu (i = 1, 2, 3)$ and the neutral vector field B_μ which couple to the weak current $\vec{J^\mu} = (J_1^\mu, J_2^\mu, J_3^\mu)$ and to the hypercharge current j_Y^μ, respectively. The two basic interactions of the electroweak lagrangian are:

$$\begin{aligned} -ig\vec{J^\mu}\cdot\vec{W}_\mu &= -ig\bar{\chi}_L\gamma^\mu\vec{T}\cdot\vec{W}_\mu\chi_L \\ -ig' j_Y^\mu B_\mu &= -ig'\bar{\psi}\gamma^\mu Y\psi \quad , \end{aligned} \tag{1}$$

where g and g' are the coupling constants, and $\vec{T}$ and Y are the generators of the $SU(2)_L$ and $U(1)_Y$ groups of gauge transformations. The χ_L's are isospin doublets of left-handed fermions while the ψ's are isospin singlets. The electromagnetic interaction appears as the combination of two neutral currents $j^\mu_{em} = J_3^\mu + \frac{1}{2}j_Y^\mu$. With the introduction in the electroweak lagrangian of a single Higgs field $\phi(x)$ as a complex scalar doublet of weak hypercharge $Y = 1$, with vacuum expectation value $\phi_0 = \sqrt{\frac{1}{2}}\begin{pmatrix} 0 \\ v \end{pmatrix}$, the gauge field mass eigenstates become:

$$\begin{aligned} W^\pm &= \frac{1}{\sqrt{2}}(W_1^\mu + W_2^\mu), \quad M_W = \frac{gv}{2} \\ Z^0 &= \cos\theta_W W_3^\mu - \sin\theta_W B^\mu, \quad M_Z = \frac{v(\sqrt{g^2+g'^2})}{2} \\ A^\mu &= \sin\theta_W W_3^\mu + \cos\theta_W B^\mu, \quad m_\gamma = 0 \quad , \end{aligned} \tag{2}$$

where θ_W is the weak angle. The weak angle relates the strengths of the weak interactions to the electromagnetic coupling e via:

$$g\sin\theta_W = g'\cos\theta_W = e \quad . \tag{3}$$

It also relates the masses of the charged and neutral weak bosons via:

$$\cos\theta_W = \frac{M_W}{M_Z} \quad , \tag{4}$$

which is a definite prediction of the SM given the particular "minimal" choice for the Higgs field.

Another prediction of the SM is that the $W^\pm$ boson has a single, universal coupling constant g to all leptons. This was true also of the G_F constant in the Fermi effective theory of electroweak interactions. The two constants are related by $g^2 = \frac{8}{\sqrt{2}}G_F M_W^2$. By inserting Eqn. 3 into the above relation, one obtains the SM prediction for the W boson mass in terms of other model parameters:

$$M_W = \left(\frac{\pi\alpha}{\sqrt{2}G_F}\right)^{\frac{1}{2}} \frac{1}{\sin\theta_W\sqrt{1-\Delta r}} \quad , \tag{5}$$

where $\alpha = e^2/4\pi$. Aside from the radiative corrections Δr and assuming the "on shell" renormalization scheme (Sirlin, 1980, and Marciano and Sirlin, 1980) which promotes the use of Eqn. 4 for all orders in perturbation theory, one can determine the W mass using three precisely measured quantities: the mass of the Z boson M_Z (Particle Data Group, 1998, p231), the Fermi constant G_F (Particle Data Group, 1998, p69), and the electromagnetic coupling constant α evaluated at $Q = M_Z$:

$$\begin{aligned} M_Z &= 91.1867 \pm 0.0021 \text{ GeV} \quad , \\ G_F &= (1.16639 \pm 0.00001) \times 10^{-5} \text{ GeV}^{-2} \quad , \\ \alpha &= (128.88 \pm 0.09)^{-1} \quad . \end{aligned} \tag{6}$$

From the measured W mass, one can derive the size of the radiative corrections Δr. Within the framework of the SM, these corrections are dominated by loops involving the top quark and the Higgs boson (see Fig. 1). The correction from the $t\bar{b}$ loop is substantial because of the large mass difference between the two quarks and is proportional to m_t^2 for large values of the top quark mass m_t. Since m_t has been measured (Particle Data Group, 1998, p347), its contribution can be calculated within the SM. For a large Higgs mass, m_H, the correction from the Higgs loop is proportional to the logarithm of m_H. In extensions to the SM, new particles may give rise to additional radiative corrections to the value of M_W. In the minimal supersymmetric extension of the standard model (MSSM), for example, additional corrections can increase the predicted W mass by up to 250 MeV (Chankowski, 1994; Garcia and Sola, 1994; Dabelstein, Hollik and Mosle, 1995; Pierce, 1997).

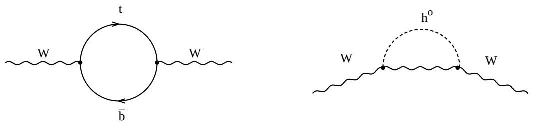

FIG. 1. Loop diagrams contributing radiative corrections to the W boson mass.

A measurement of the W mass therefore constitutes a test of the SM. Together with a measurement of the top quark mass, the SM predicts M_W up to a 200 MeV uncertainty due to the unknown Higgs mass. By comparing the calculation to the measured value of the W mass, one can constrain the mass of the Higgs which has not yet been detected experimentally. A discrepancy with the range allowed by the SM could indicate new physics. The experimental challenge is thus to measure the W mass to sufficient precision, about 0.05%, to be sensitive to these corrections. The CDF and DO experiments at the Tevatron Collider have recently performed direct measurements of the W mass approaching this level of precision, as we will see in Sec. V.A.

The W width Γ_W is precisely predicted in the SM in terms of the mass and coupling of the W boson. Its value is extracted from the ratio $\Gamma_W = \Gamma(W \to l\nu)/B(W \to l\nu)$ where $\Gamma(W \to l\nu)$ is the leptonic partial width and $B(W \to l\nu)$ the leptonic branching ratio ($l = e$ or μ). The former can be expressed in the SM as:

$$\Gamma(W \to l\nu) = \frac{G_F M_W^3}{6\sqrt{2}\pi(1+\delta)} \tag{7}$$

where δ is the radiative correction to the Born-level calculation and is less than 0.5%. The latter is:

$$B(W \to l\nu) = \frac{1}{3 + 6(1 + \alpha_s(M_W)/\pi) + \mathcal{O}(\alpha_s^2)} \tag{8}$$

to first order in the strong coupling constant α_s evaluated at the renormalization scale $Q = M_W$. The first term in the denominator is due to the three ($e\nu$, $\mu\nu$ and $\tau\nu$) leptonic decay modes, assuming lepton universality and ignoring small phase space effects. The second term is due to the hadronic decay to the first two generations of quarks $u\bar{d}$ and $c\bar{s}$, with a QCD color factor of 3 and the first-order QCD gluon radiative correction. From Eqns. 7 and 8, the SM numerical prediction for the total W width is $\Gamma_W = 2.093 \pm 0.002$ GeV. The consistency of early measurements of Γ_W with this SM prediction was used to prove that if the top quark was the weak isospin partner of the bottom quark, then the absence of the $W \to t\bar{b}$ partial width implied a lower limit on the top mass $m_t > M_W - m_b$ (Abe *et al.*, 1995g).

The W width can also be determined indirectly by using the ratio

$$R \equiv \frac{\sigma_W \cdot B(W \to l\nu)}{\sigma_Z \cdot B(Z \to l^+l^-)} \tag{9}$$

where σ_W and σ_Z are the inclusive cross sections for W and Z production, and B are the respective leptonic branching ratios. By measuring R, the branching ratio $B(W \to l\nu)$ can then be extracted as

$$B(W \to l\nu) = R\frac{\sigma_Z}{\sigma_W}B(Z \to l^+l^-) \tag{10}$$

where $\frac{\sigma_Z}{\sigma_W}$ can be calculated theoretically, and $B(Z \to l^+l^-)$ has been measured precisely at LEP. The total W width is then derived by using the SM calculation of $\Gamma(W \to l\nu)$. Sections V.B and V.C will review the Tevatron results on Γ_W and the limits on the W partial width into new decay modes.

The measurements of $\sigma_W \cdot B(W \to \tau\nu)$ and $\sigma_W \cdot B(W \to e\nu)$ provide a test of lepton universality since their ratio can be expressed as:

$$\frac{\sigma_W \cdot B(W \to \tau\nu)}{\sigma_W \cdot B(W \to e\nu)} = (\frac{g_\tau}{g_e})^2 \quad . \tag{11}$$

The universality of the leptonic couplings to the weak charged current is a direct consequence of the assumption that the leptons transform as $SU(2)_L$ doublets.

Another important prediction of the SM, due to the non-abelian character of the $SU(2)_L$ isospin symmetry group, is the existence of three and four vector boson vertices. Gauge invariance uniquely determines the structure of these W, Z and γ boson self-coupling terms. In the SM, only $WW\gamma$ and WWZ vertices are predicted to exist at tree level. The other possible triboson combinations, $ZZ\gamma$, $Z\gamma\gamma$ and ZZZ, are not allowed because the couplings of particles to the Z boson depend on their electric charge and weak-isospin, both of which are zero for the neutral bosons. Studies at $p\bar{p}$ machines of $W\gamma$, WW and WZ production rates and kinematical distributions provide a direct measurement of the trilinear W couplings via the s-channel γ and Z exchange interactions (see Fig. 2). Such direct measurements provide a very powerful test of the gauge structure of the SM because even a small deviation of the trilinear couplings from their predicted values will greatly affect the subtle cancellation among the three contributions of Fig. 2 which is needed to control the unitarity of the process.

In studying possible deviations from the SM predictions one assumes that the new physics responsible for such deviations manifests itself at an energy scale Λ not yet reached by present accelerators. Such new particles will affect the triboson vertices via loop-diagram contributions and can be studied by introducing an effective lagrangian formalism which parametrizes the contributions of new physics via a set of unknown constants.

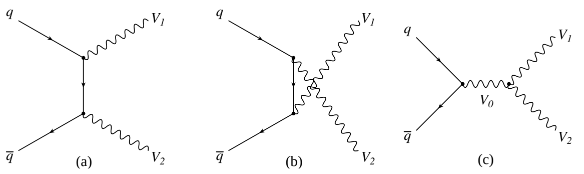

FIG. 2. Tree-level Feynman diagrams for vector boson pair production: (a) t-channel diagram; (b) u-channel diagram; (c) s-channel diagram. For $W\gamma$ production $V_0 = V_1 = W$ and $V_2 = \gamma$. For WW production $V_0 = \gamma$ or Z, $V_1 = W^+$ and $V_2 = W^-$. For WZ production $V_0 = V_1 = W$ and $V_2 = Z$.

The most general effective lagrangian for WWV couplings ($V = Z$ or γ) consistent with Lorentz invariance can be expressed in terms of 14 dimensionless coupling parameters (Hagiwara *et al.*, 1993) g_1^V, κ_V, λ_V, g_4^V, g_5^V, $\tilde{\kappa}_V$, and $\tilde{\lambda}_V$. After imposing P, C and CP symmetry, only the g_1^V, κ_V and λ_V parameters are non-zero. Furthermore $g_1^\gamma = 1$ due to the gauge invariance of the electromagnetic interaction. To regain the SM lagrangian, one must set $g_1^Z = 1$, $\Delta\kappa_V \equiv \kappa_V - 1 = 0$ and $\lambda_V = 0$. Any deviation from these "effective" couplings will be an indication of anomalies in the WWV vertex. For example, in the case that the γ couples only to the electric charge of the W boson, which is called minimal $U(1)_{EM}$ coupling, we would expect the "anomalous" values of $\Delta\kappa_V = -1$ and $\lambda_V = 0$. For the present experimental limits and theoretical estimates of the coupling parameters see the review by Ellison and Wudka (1998).

The effective lagrangian violates unitarity at energies approaching the scale of new physics, Λ. The anomalous couplings are then modified by form factors dependent on the scale Λ. A commonly used expression for such form factors is $\lambda_V(\hat{s}) = \frac{\lambda_V^0}{1+\hat{s}/\Lambda^2}$ where $\hat{s}$ is the squared center-of-mass energy of the scattering process. This choice, unlike the rest of the effective lagrangian formalism, is model-dependent. Experimentally Λ is chosen to be close to the maximum value allowed by unitarity constraints. In Sec. V.H we present limits on anomalous couplings obtained by the CDF and DO experiments at the Tevatron.

B. Role of the W Boson in Quantum Chromodynamics

W bosons, in addition to providing a powerful probe of electroweak physics, also provide a means to study QCD through measurements of their production properties. Unlike quarks and gluons, W (and Z) bosons are colorless and do not hadronize. Thus by selecting their decays into leptons, they act as direct probes of the hard partonic processes. In addition, their large mass allows most of their production properties to be calculated perturbatively in QCD.

Perturbative QCD can be probed in a variety of ways using W and Z bosons, the most inclusive one being the total production cross section. Typically this is expressed as the leading order Born cross section times a multiplicative factor K which embodies the effect of next-to-leading-order (NLO) processes involving initial state quark and gluon radiation (see Eqn. 12). As discussed in Sec. V.C, comparisons of measurements with calculations show good agreement.

The p_T spectrum of the bosons provides another probe of QCD processes and can be calculated reliably at high p_T using perturbative methods. At low boson p_T, resummation and non-perturbative techniques are needed to adequately describe the data, as described in Sec. II.A. The value of the strong coupling constant α_s enters the calculation of the production cross sections for the number of jets produced in W and Z events. NLO QCD predictions (Giele, Glover, and Kosower, 1993) for $W + \geq 0$ or ≥ 1 jet allow a parameterization of the cross section as $\alpha_s^n(A_n + \alpha_s B_n)$ where n is 0 or 1. By using the ratio of these cross sections, one can cancel many uncertainties in the experimental measurements and theoretical predictions. The data can be compared to the predictions for different values of the renormalization scale. These measurements are discussed in detail in Sec. V.E.

Another approach to studying QCD is to use the angular distributions of the jets in W or Z events. In W + 1 jet events, where the production matrix elements are dominated by quark propagators, the W boson or the jet is expected to have a polar angle distribution of $dN/d\cos\theta^* \sim (1 - |\cos\theta^*|)^{-1}$ due to the spin-1/2 propagator. In comparison, in gluon-propagated dijet events, the integral spin of the gluon results in an inverse square dependence of the angular distribution.

These techniques provide a clean window with which to observe and measure perturbative QCD effects. Non-perturbative QCD in the form of the parton distribution functions (PDFs), can also be studied. Every process that occurs at a hadron collider is subject to the influence of the PDFs. The uncertainties in the PDFs affect every analysis and, in the case of the measurement of the W mass, play a significant role in the total uncertainty. Since the rapidity distribution of the W boson is sensitive to the product of the PDFs of the quarks and antiquarks, a measurement of the W rapidity helps to constrain the PDFs, in particular the ratio of the d quark to u quark distributions, $\frac{d}{u}$ (Berger *et al.*, 1989; Martin, 1989) in a complementary fashion to deep inelastic scattering and Drell-Yan measurements. Unfortunately, one cannot reliably reconstruct the rapidity of the W because of the presence of the neutrino in the decay. The experimental observable used is the lepton forward-backward charge asymmetry, usually just referred to as the W charge asymmetry, which is a convolution of the true W forward-backward charge asymmetry and the forward-backward charge asymmetry of the $V-A$ leptonic decay of the W boson, the latter being understood very well from muon decay experiments. The measurement of the W asymmetry is described in Sec. V.D.

C. Role of the W Boson in Non-Standard Model Physics

Measurements of the W and Z properties provide a means of searching for new heavy particles decaying to these bosons. For instance, if a new heavy particle were to decay to a W or Z boson and anything else, the boson p_T distribution would show an excess above the QCD prediction. W and Z have similar production dynamics but different decay modes so they provide complementary measurements. Other studies of the properties of jets accompanying W and Z bosons are important not only because they provide tests of LO and NLO QCD predictions but also because production of $W/Z+$ jets is often a significant background to Higgs searches or other new physics processes. In Section V.E we will review the studies of QCD-related vector boson production properties performed at the Tevatron.

Section V.F will report on direct searches for additional heavy gauge bosons, which arise in extensions of the SM aimed at restoring the left-right symmetry of the electroweak lagrangian (Mohapatra, 1992). Such models replace the $SU(2)_L \times U(1)_Y$ symmetry group with an extended $SU(2)_R \times SU(2)_L \times U(1)_Y$, thus introducing two new charged $W_R^{\pm}$ and one neutral Z' gauge bosons along with massive right-handed neutrinos ν_R. The decay of a right-handed W_R into WZ will be suppressed by the left-right mixing angle $\xi \sim (M_W/M_{W_R})^2$ (Ramond, 1983). If the W_R is heavy enough, its decay into right-handed $l_R\nu_R$ pairs becomes dominant. In models with manifest left-right symmetry the strength of the coupling of the right-handed bosons to left and right-handed fermions becomes the same and equal to the SM values. This is also referred to as the "standard coupling" scenario. Indirect limits on the W_R mass can be inferred from low energy phenomena like deviations of the V-A angular distribution in polarized muon decays, measured difference between the K_S and K_L masses and neutrinoless nuclear double beta decay. The above limits are combined to exclude a heavy W_R boson below 1.3 TeV (Langacker, 1989). Cosmological constraints (Olive *et al.*, 1981; Raffaelt *et al.*, 1988; Barbieri *et al.*, 1989) have established limits of $\mathcal{O}$(1-10) TeV assuming very low neutrino masses ($M_{\nu_R} <$ 1-10 MeV).

The study of rare W decays also provides a window on new physics. Physics beyond the SM often brings with it the existence of new particles that, while too heavy to be observed as real particles, appear as virtual particles in lower energy processes, thus altering cross sections and decay rates. In searches for rare W decays at the Tevatron, one concentrates on easily identifiable low-background final states and looks for the enhancement of decay rates to observable levels well above those predicted by the SM. The present status of these searches is reviewed in Sec. V.G.

II. W PRODUCTION IN $p\overline{p}$ COLLISIONS

In $p\overline{p}$ collisions at $\sqrt{s}$ = 630 GeV at the S$p\overline{p}$S collider and $\sqrt{s} = 1.8$ TeV at the Tevatron collider, W and Z bosons are produced mainly through quark-antiquark annihilation. Figure 3 shows the lowest-order diagrams.

A. W and Z Boson Production and Decay

Due to the large mass of the W and Z bosons, QCD factorization can be employed to calculate their production cross sections in hadron collisions. The lowest order cross section can be written as

$$\frac{d^2\sigma}{dp_T^2 dy} = \sum_{q,\bar{q}} \int dx_1 \int dx_2 f_q(x_1,\hat{s}) f_{\bar{q}}(x_2,\hat{s}) \delta(sx_1x_2 - \hat{s}) \frac{d^2\hat{\sigma}_{q,\bar{q}}}{dp_T^2 dy} \quad , \tag{12}$$

where $\hat{\sigma}$ is the partonic cross section, and f_q, $f_{\bar{q}}$ are the parton distribution functions for the annihilating quarks. p_T and y are the transverse momentum and rapidity of the vector boson respectively. x_1 and x_2 are the proton momentum fractions carried by the annihilating quarks, and $\hat{s}$ is the partonic center-of-mass energy squared. $\hat{\sigma}$ is given by the relativistic Breit-Wigner lineshape with $\hat{s}$-dependent width

$$\frac{d\hat{\sigma}}{d\sqrt{\hat{s}}} = \frac{\hat{s}}{(\hat{s}-M_W^2)^2 + (\frac{\hat{s}\Gamma_W}{M_W})^2} \quad . \tag{13}$$

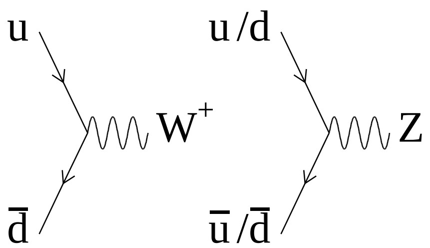

FIG. 3. Lowest order production diagrams for W and Z bosons in a hadron-hadron collision.

Due to the $V-A$ nature of the weak interaction, the W spin is aligned with the direction of the incoming antiquark at lowest order. At the Tevatron energy, approximately 80% of the time, a valence quark from the proton or the antiproton is involved in the reaction. This means that roughly 80% of the time, the W spin is aligned with the antiproton direction of motion. The remaining 20% of the time, the W boson is produced from two sea quarks, and the boson's spin is equally likely to be parallel or antiparallel to the proton's direction. This leads to a significant experimentally observable forward-backward asymmetry between W^+ and W^- production, as we discuss in Sec. V.D. Figure 4 details the kinematics of the process and shows both the lepton forward-backward charge asymmetry and the contribution from just the W forward-backward asymmetry. The two asymmetry contributions (W and $V-A$ decay) are of opposite sign. The $V-A$ asymmetry is small at low rapidity but increases with rapidity and tends to cancel the W asymmetry at the highest values of rapidity accessible to the detector.

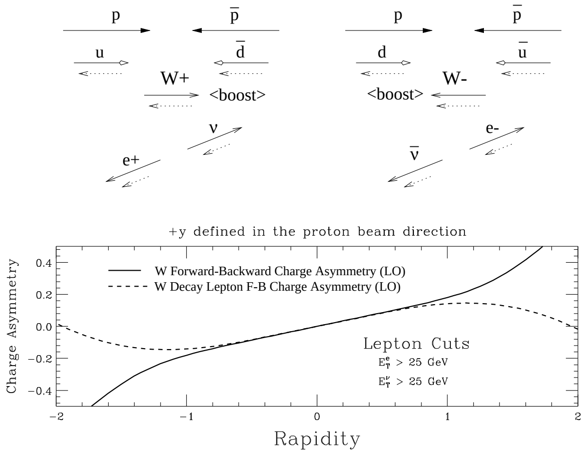

FIG. 4. Top: The kinematics of W production showing components relevant to the W forward-backward asymmetry measurement. The solid lines indicate momentum flow and the dashed lines indicate spin. The PDFs cause the $W^+(W^-)$ to be boosted in the direction of the $p(\overline{p})$. Bottom: The true W asymmetry (solid) and the sum of W and $V-A$ asymmetries (dashed).

The decay channels open to the W boson are the three lepton channels ($e\nu_e$, $\mu\nu_\mu$ and $\tau\nu_\tau$) and two hadronic channels, $u\bar{d}$ and $c\bar{s}$ [1]. Due to the three-fold color degeneracy of the quarks, the hadronic channels account for 2/3 of the W decay branching ratio, and each leptonic channel accounts for 1/9 of the branching ratio, neglecting small quark and lepton mass corrections.

Inclusive production of W bosons and their subsequent decay into quarks is dwarfed in production cross section by inclusive QCD dijet production. Hence an inclusive W signal in the dijet channel is extremely difficult to identify. This is particularly true of the Tevatron where dijet production through initial state gluons has a large contribution for dijet mass near the W mass. At the S$p\overline{p}$S the gluon contribution was lower, allowing the dijet mass "bump" due to W (and Z) decay to be visible (Ansari *et al.*, 1987b).

When the W decay axis is perpendicular to the beam axis (which occurs a large fraction of the time since the phase space peaks at 90°), the decay leptons have large transverse momentum due to the large W mass. Most particles produced in the interaction of the proton (and antiproton) remnants have relatively low transverse momentum. Hence one expects low transverse energy flow in the immediate vicinity of the lepton, a property often referred to as energy isolation. The neutrino from the W decay interacts only through the weak interaction, and therefore for practical purposes is invisible to the detectors. The remnants of the beam particles are emitted at very small angles and typically travel down the beam pipes undetected, thereby producing an inherent longitudinal momentum imbalance. However, most of the energy emitted at large angles is detected by building detectors with extensive coverage of the total solid angle. Hence, by measuring the total detected transverse momentum and requiring balance, the neutrino transverse momentum can be inferred.

At lowest order, the angular distribution of the lepton from the W decay is governed by the $V-A$ interaction

$$\frac{d\sigma}{d\cos\theta^*} \propto (1-\lambda q\cos\theta^*)^2 \quad , \tag{14}$$

where λ is the helicity of the W boson with respect to the proton direction, q is the charge of the lepton, and θ^* is the angle between the charged lepton and proton beam directions in the W rest frame. Quark and gluon radiation in the initial state has two effects on the W polarization in the laboratory frame. Firstly, there is a kinematic effect because the W spin axis is no longer the beam axis, rather it is now rotated with respect to the beam axis. Secondly, there is a dynamical effect on the initial state angular momentum because the radiated partons are spin 1/2 quarks and spin 1 gluons. These effects modify the W angular distribution with respect to Eqn. 14 in a way that depends on the W transverse momentum (p_T^W)

$$\frac{d\sigma}{d\cos\theta_{\rm CS}} \propto \left(1-\lambda q\alpha_1\cos\theta_{\rm CS}+\alpha_2\cos^2\theta_{\rm CS}\right) \quad , \tag{15}$$

where the coefficients α are functions of p_T^W. A QCD calculation of these coefficients has been carried out (Mirkes,

[1]Here we are referring to the weak interaction eigenstates rather than the cabibbo-rotated mass eigenstates.

Willfahrt and Zeppenfeld, 1997) at order α_s^2. These calculations are performed in the Collins-Soper frame (Collins and Soper, 1981), and θ_{CS} is the W decay angle in this frame.

The leading order QCD processes that generate p_T^W are shown in Fig. 5. When p_T^W is large, i.e. comparable to the W mass, the perturbative QCD calculation can be expressed as a power series in α_s. The differential cross section in p_T^W has been computed by Arnold and Reno (1989).

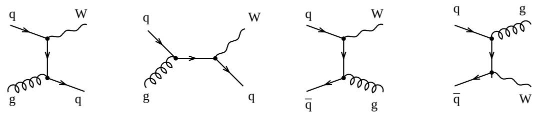

FIG. 5. The leading order QCD diagram for initial state gluon radiation accompanying W production.

The fixed order (in α_s) perturbative QCD calculation becomes invalid at low values of p_T^W. This can be understood as follows. The virtuality of the internal propagator is of order p_T^W. As p_T^W reduces the propagator tends to diverge. Multiple initial state parton radiation becomes favorable because the reduction in the cross section due to each power of α_s is more than compensated by the divergence of the additional propagator. The divergence of the propagators is manifested in the perturbative calculation as terms of the form $\log(M_W/p_T^W)$. It can be seen that the most divergent term at each order in α_s has the form $[\alpha_s \log(M_W/p_T^W)]^n$, the second-most divergent term is of the form $\alpha_s^n \log^{n-1}(M_W/p_T^W)$ and so on. By rearranging the terms of the perturbative expansion and summing certain sets of terms, the cross section can be expressed as a power series in $[\alpha_s \log(M_W/p_T^W)]$. This technique is called resummation (Collins, Soper and Sterman, 1985), and the collection of the leading logarithmic divergence at each order leads to the leading-logarithmic approximation, or LLA. Physically, this corresponds to the summing over the most important contributions from multiple gluon emission diagrams.

The resummed form of the differential cross section in p_T^W is often expressed as a fourier transform in the space of the impact parameter b,

$$\frac{d^2\hat{\sigma}}{dp_T^2 dy} \approx Y(b,Q) + \int_0^\infty d^2b e^{i\vec{p}_T\cdot\vec{b}} W(b,Q) \quad , \tag{16}$$

where W is the resummed piece and Y is a correction based on the fixed order perturbative result. Y attempts to correct for terms present in the fixed order calculation which were left out in the resummation procedure. W can be expressed as $W(b,Q) \sim e^{S(b,Q)}$, where $S(b,Q)$ is called the Sudakov form factor.

The resummation technique is a reformulation of the perturbative QCD expansion, and extends the applicability to lower p_T^W values. While nature makes a smooth transition from the high p_T regime (where fixed order calculations are most valid) to the intermediate p_T range where resummation calculations are more valid, this transition has not yet been fully described by rigorous QCD calculations. The transition is approximated in the p_T^W range of 30-50 GeV.

At very low p_T^W values, i.e. below $\sim$10 GeV, the perturbative expansion itself becomes invalid, and non-perturbative phenomenological models need to be applied. These models introduce a non-perturbative form factor to cut off the divergence in the QCD calculation as $p_T \to 0$

$$W(b,Q) \to W(b^*,Q)e^{-S_{NP}(b,Q)}, \tag{17}$$

where

$$b^* = \frac{b}{\sqrt{1+(b/b_{max})^2}} \tag{18}$$

and b_{max} is chosen in the range 0.5/GeV. S_{NP} is a non-perturbative function with the properties $S \to 0$ as $b \to 0$ and $S \to \infty$ as $b \to \infty$. It has been shown to have the form

$$S_{NP}(b,Q) = h_1(b,x_q) + h_1(b,x_{\bar{q}}) + h_2(b)\ln(\frac{Q}{2Q_0}), \tag{19}$$

where x_q and $x_{\bar{q}}$ are the momentum fractions of the annihilating quarks, Q_0 is an arbitrary momentum scale, and $h_1(b,x_q)$, $h_1(b,x_{\bar{q}})$ and $h_2(b)$ are empirical functions to be determined from experiment. In the model of Ladinsky and Yuan (1994), these functions are given by

$$\begin{aligned} h_2(b) &= g_2 b^2 \\ h_1(b,x_q) + h_1(b,x_{\bar{q}}) &= g_1 b^2 + g_1 g_3 b \ln(100 x_q x_{\bar{q}}). \end{aligned} \tag{20}$$

These functions provide Gaussian smearing of the transverse momentum. The g parameters are determined by fitting Drell-Yan data.

B. Underlying Event

The hard scattering of two partons in a $p\overline{p}$ collision leaves behind the remnants of the proton and the antiproton to form one component of the underlying event. These remnants, as explained in Section II.A, are mostly directed forward and backward along the beam line although a few follow a transverse course, resulting in a low level background of particles in all events. The charged particle multiplicity per unit pseudorapidity is $\sim$ 4 at Tevatron energies and logarithmically increases with center-of-mass energy (Abe *et al.*, 1990a).

Another component of the underlying event results from additional $p\overline{p}$ interactions occurring during the same bunch crossing as the hard scatter. In each crossing, the number of $p\overline{p}$ interactions follows a Poisson distribution, of which the mean, $\bar{N}$, is a function of the instantaneous luminosity ($\mathcal{L}$) and the number of bunches (N_b): $\bar{N} = \mathcal{L}\sigma T/N_b$ (T is the time for the bunches to travel around the collider, and σ is the $p\overline{p}$ cross section). For a given $\mathcal{L}$, the larger N_b is, the less dense each bunch is and the fewer the number of additional interactions that will occur.

C. Modelling of W Boson Production

Processes involving W bosons are typically modelled using a Monte Carlo simulation which varies in detail depending on the species and precision of the measurement. There are two principal parts to the modelling: an event generator, and a detector simulation.

1. Event generation

Event generators come in two kinds: leading-order (LO), which may or may not attempt some form of next-to-leading-order QCD and/or QED corrections; and next-to-leading-order (NLO) calculations. A complete NLO calculation which is reliable over the broad range of W boson physics at hadron colliders does not exist. However, there are a number of partial calculations and various other techniques that can be used to achieve the required precision for any given measurement.

All flavors of event generator use a matrix element calculation convoluted with PDFs (Eq. 12). The PDFs are probability densities for a given parton to be carrying a given fraction of the proton's momentum. They are measured mostly from deep inelastic scattering, Drell-Yan and direct photon measurements with an important contribution from the W charge asymmetry measurement (see Sec. V.D).

The matrix element depends on the generator. LO generators start with the tree level s-channel subprocess (Eq. 13) and add NLO effects afterward. The NLO generators start with a matrix element which is usually not true NLO. Instead, it contains certain NLO features of relevance for the particular generator. For example, an NLO QED generator may not contain any QCD effects and in fact it may have only parts of the complete NLO QED corrections. This leads to many different event generators each of which deal with certain specific cases.

As stated above, LO generators need two corrections: QCD corrections corresponding to initial state radiation off the incoming partons (and for a few analyses off the outgoing quarks as well), and QED corrections dealing with radiation off the final state leptons. Initial state QCD radiation causes transverse momentum (p_T^W) to be imparted to the W boson, and appears as "jet(s)" of hadrons descending from the radiated parton(s). The initial state radiation is calculated in a variety of ways. The popular event generators ISAJET (Paige and Protopopescu, 1986), PYTHIA (Sjostrand, 1985; Sjostrand and van Zijl, 1987), and HERWIG (Marchesini and Webber, 1988) introduce radiation off the incoming partons using the QCD Altarelli-Parisi splitting function and then "hadronize" the resulting parton shower into observable particles. The low-energy cutoff for the radiated partons in these generators is around 1 GeV (6 GeV for ISAJET) where perturbative QCD begins to fail. At lower p_T^W values, non-perturbative parameters such as intrinsic p_T of initial-state partons are introduced.

Another option is to use either a measured p_T^W distribution or a calculation of p_T^W and simply boost the W decay products by hand. The recoiling hadrons are not generated. Several p_T^W calculations have been published (Ladinsky and Yuan, 1994; Ellis and Veseli, 1998), as well as a calculation of the ratio of p_T^W to p_T^Z distributions (Giele and Keller, 1998). These calculations are doubly differential in p_T^W and rapidity. The absolute p_T^W calculations utilize the technique of matching perturbative QCD at large p_T^W to a resummation calculation coupled with a non-perturbative form factor at low p_T^W. For the non-perturbative form factor, Ladinsky and Yuan integrate over impact parameter space while Ellis and Veseli integrate over momentum space. Both calculations yield similar results. The nonperturbative part involves an ad-hoc parameterization with parameters that need to be determined from collider and lower-energy data. Some of these parameters vary with the choice of PDF. In the ratio of the p_T^W to the p_T^Z distribution, large contributions from the non-perturbative and resummation regions cancel.

The second correction needed for a LO subprocess is a QED correction involving three possibilities: photon radiation off the initial state partons, the final state lepton, and the W propagator. The PHOTOS Monte Carlo (Barberio and Was, 1994) can generate multiple photon emissions (using LLA) off the final state lepton and is often used in conjunction with other generators. It does not compute initial state radiation or radiation off the propagator.

As with QCD corrections, NLO QED calculations also exist which include all or parts of the relevant diagrams. The calculation by Berends and Kleiss (1985) includes the final state radiation and the half of the propagator radiation that cancels the divergences in the final state radiation. This corresponds essentially to corrections to W decay and is especially useful in the mass measurement where the final state radiation changes the measured mass.

The calculation by Baur and Berger (1990) includes all the diagrams but treats the initial and final state particles as massless using an energy cutoff to control divergences. Recently, an improved true NLO electroweak calculation

(Baur, Keller and Wackeroth, 1999) has become available including diagrams to $\mathcal{O}(\alpha^3)$.

2. Detector simulation

The second half of modelling involves the effect of the detector on the event. Usually this consists of some combination of detailed traces through the detector of every particle in the event and parameterizations of the salient features of the event.

Detailed trace simulations such as GEANT (Brun *et al.*, 1978) follow every particle, including any daughters from decays and material interactions, through the detector, accounting for energy losses in the material and simulating the detector signals. This process continues until the particles annihilate or reach some minimum energy. The conversion from energy losses to the simulated data is usually tuned to agree with real data. This form of detector simulation is generally slow and is sometimes sped up by the inclusion of parameterizations of certain aspects. For example, a particle's momentum is obtained not from fitting hits from the tracking chamber, but from smearing the momentum delivered by the generator. In analyses where speed is critical, such as the W mass measurement, nearly all parts of the simulation are parameterized.

Among the parameterizations, the most complicated to constrain is the detector response to the "recoil jets" of hadronized particles from initial state radiation. Since the energy of the initial state radiation is relatively low (mean of 5-10 GeV), the particle energies in the recoil are often only hundreds of MeV. This results in a poor response in the calorimeter which is usually calibrated for much higher energy particles. For experiments with a central magnetic field, some of these particles are lost as they orbit in the magnetic field at a radius smaller than the calorimeter.

Typically, the parameterization of the recoil, $\vec{u}_T$, is separated into response and resolution components both of which may be a function of the boson p_T,

$$\vec{u}_T = -\vec{p}_T^{\,W} \cdot \mathcal{R}(p_T^W) \oplus \vec{\sigma}(p_T^W) \quad . \tag{21}$$

The exact form of $\mathcal{R}$, which incorporates the mean response, and σ, which provides the resolution fluctuations, depends on details of the detector.

Both the response and resolution functions may be constrained by using jet, direct photon and/or Z events. With a magnetic tracker, reconstructed tracks can be used to calibrate the calorimeter response. Direct photon or Z events can also be used to constrain the hadronic response and resolution by comparing the measured recoil with the measured E_T^γ or p_T^Z as determined from the daughter leptons of the Z boson, and assuming there is no true $\not\!\!E_T$ in these events. This technique carries an assumption that the initial state radiation hadronizes in the same manner independent of the brand of vector boson produced in association with it.

Another simulated element related to the recoil is the underlying event. This is usually parameterized as a function of the instantaneous luminosity by using soft inelastic collisions called minimum bias events[2]. The effect of these soft collisions is to degrade the resolution and shift the mean of the recoil measurement. It also alters the energy measurement of electrons and decreases the efficiency of any lepton identification requiring energy isolation since there is more energy everywhere in the event, including near the lepton.

Electron energy measurements are simulated using a parameterization obtained mostly from testbeam data. Depending on the measurement, the electron simulation may also include the effects of the underlying event and additional constraints from physics data, such as an energy scale constraint from known mass resonances.

III. DETECTION OF W BOSONS IN $p\overline{p}$ COLLISIONS

The challenge for detectors at $p\overline{p}$ colliders is to extract physics signatures with typical cross sections as small as a few nanobarns, or even picobarns, from the total $p\overline{p}$ cross section which is many orders of magnitude larger. To set the scale, during the 1990-1996 run of the Fermilab Tevatron accelerator (Run 1), protons and antiprotons were colliding at a center of mass energy of 1.8 TeV, resulting in a $p\overline{p}$ inelastic cross section of about 50 mb (Particle Data Book, 1998, p 206). At this energy, W bosons are produced with a cross section of approximately 20 nb, i.e. once every 250,000 $p\overline{p}$ collisions. To achieve these huge rejection factors, the detectors must be designed with sophisticated multi-level trigger systems.

Two detectors were run in parallel during the Run 1 of the Tevatron: CDF (Abe *et al.*, 1988) and DO (Abachi *et al.*, 1994), whose schematic views can be found in Figs. 6 and 7 respectively. Both detectors aimed at identifying particles coming out of the interaction region over the largest possible $\eta \times \phi$ area [3]. During Run 1 the luminous region was about ± 35 μm (r.m.s.) in radius and ± 33 cm (r.m.s.) in length along the beam axis. CDF measured the p_T of charged particles with a resolution of $\sigma(p_T)/p_T \approx \sqrt{(0.9 p_T)^2 + (6.6)^2} \times 10^{-3}$ (p_T

---

[2] The term "minimum bias" is used because of the minimal selection requirements placed on the event, usually a coincidence of hits from scintillators placed near the beamline to catch the remnants of the proton and the antiproton.

[3] The pseudorapidity η is defined as $\eta = -\log[\tan\theta/2]$ where θ is the polar angle with respect to the beam axis. The azimuthal angle ϕ is measured in the plane perpendicular to the beam axis.

in GeV/c) in the region of $|\eta| < 1.1$ due to a system of tracking chambers immersed in a magnetic field of $B = 1.4$ T. Outside the solenoid were electromagnetic and hadronic sampling calorimeters divided into central ($|\eta| < 1.1$), endcap ($1.1 < |\eta| < 2.4$) and far-forward regions ($2.2 < |\eta| < 4.2$). They provided an energy resolution of $\sigma(E)/E \approx \sqrt{(14\%)^2/E + (1.5\%)^2}$ for central electrons and $(\sigma(E)/E) \approx (70\%)/\sqrt{E}$ for central pions (E in GeV). The outermost instrumented area was designed to detect muons using a combination of drift chambers and scintillators.

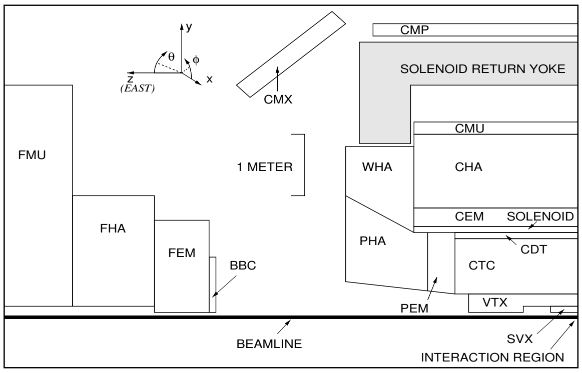

FIG. 6. Cross-section view of the CDF detector. The tracking system is comprised of SVX, VTX, CTC and CDT. The central, plug and forward calorimeters are CEM/CHA, PEM/PHA+WHA and FEM/FHA for the electromagnetic and hadronic part respectively. The muon detectors are CMU, CMP, CMX and FMU.

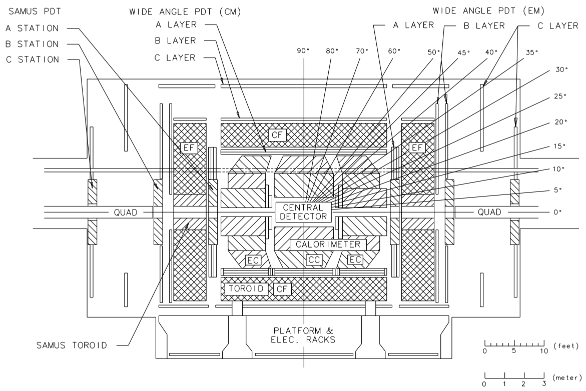

FIG. 7. Cross-section view of the DO detector. The tracking is done in the central detector. Central and endplug calorimeters are CC and EC respectively. The muon system consists of CF, EF, SAMUS proportional drift tube (PDT) systems.

The DO inner tracking chamber was divided into central and forward portions and covered the region $|\eta| < 3.2$. Lacking an inner magnetic spectrometer, DO relied upon calorimetric information for electron and jet energies. Its uranium-liquid argon calorimeter was designed to have better hermiticity and stability and finer segmentation than CDF in the region $|\eta| < 4.4$ and provided an energy resolution of $\sigma(E)/E \approx \sqrt{(13.5\%)^2/E_T + (1.1\%)^2}$ for central electrons, $\sigma(E)/E \approx \sqrt{(15.7\%)^2/E_T + (1.0\%)^2}$ for forward electrons and $\sigma(E)/E \approx 50\%/\sqrt{E_T}$ for pions. The muon system consisted of toroid magnets between layers of drift tubes, and was able to measure the muon momentum with a resolution of $\sigma(p_T)/p_T^2 \approx 20\%$ over the region $|\eta| < 3.3$.

A. Triggering of W boson events

Leptonic W decays are characterized by a single, isolated, high p_T lepton, either an electron or a muon, and large $\not{E}_T$ indicative of the decay neutrino. The decay into a single τ lepton is less commonly pursued in $p\overline{p}$ machines because of the additional complication of having to reconstruct the τ through its decay products (Abbott *et al.*, 2000e; Abe *et al.*, 1992a). The Z boson is widely used to provide control samples in studies of the W properties. As with W decays, the Z hadronic decays are similarly difficult to disentangle from the QCD background on an event-by-event basis. Its decays into a pair of charged leptons are relatively easy to identify by requiring an isolated, high p_T lepton accompanied by a second lepton instead of $\not{E}_T$. Studies involving diboson production and rare W decays benefit from the identification of a photon, a jet or additional leptons in the event. In the following sections we will present the strategies used by detectors at the Tevatron for triggering and reconstructing each of the W and Z decay products.

B. Electron detection

Electrons are identified as clusters of adjacent calorimeter cells with significant energy deposit in the electromagnetic section of the calorimeter. The lateral segmentation of the calorimeter is usually such that the electron deposits most of its energy in a single calorimeter tower. In DO for example, clusters with at least 90% of their energy in the electromagnetic section and at least 60% of their energy in the most energetic calorimeter tower are considered as electron candidates. Any sample of events selected solely on the basis of the above criteria will contain a sizeable fraction of events with an isolated high energy photon. The additional requirement of a track pointing to the calorimeter cluster separates very effectively the electron from the photon contribution.

The electron identification can be further refined by comparing the transverse and longitudinal energy deposition profile in the calorimeter to typical shower shapes obtained from test-beam studies with electrons. Limiting the amount of energy that leaks into the hadronic calorimeter and requiring a track matching the cluster in position and energy reduces the probability of a hadron being misidentified as an electron. Isolation quantities such as the amount of energy detected in areas surrounding the electron shower are helpful in rejecting events with electrons/photons inside a jet.

C. Muon detection

Muons typically interact with small energy loss in the material inside the detector whereas most other particles interact heavily and are stopped in the calorimeter. A muon signature is therefore a charged track in the central tracking chamber pointing to hits in dedicated chambers placed outside the calorimeter, coupled with an energy deposition in the calorimeter consistent with a minimum ionizing particle.

By constraining the track to come from the beam interaction point, which is inferred from the common origin of all the tracks in the event, one substantially improves the muon track parameter resolution and rejects cosmic rays. To reject misidentified backgrounds from energetic punch-through pions which deposit only a small fraction of their energy in the calorimeter before escaping, one can increase the isolation of the muon beyond its immediate vicinity since the punch-through pions are generally part of a non-isolated jet environment. Real muons from pion decay in flight or b-quark, c-quark semileptonic decays are also part of a non-isolated jet environment and rejected by similar cuts.

D. Neutrino detection

The recoil energy $\vec{u}_T$ is calculated as the vector sum of the transverse energies deposited over all the calorimeter towers, except for the ones that contain energy coming from the lepton in W decays. Such $\vec{u}_T$ is a measure of the transverse energy of the partons recoiling against the W boson in processes shown in Fig. 5. The underlying event is expected to be distributed symmetrically in the transverse plane and therefore their contribution to $\vec{u}_T$ should be zero on average. By momentum conservation, the neutrino transverse energy $\vec{\not{E}}_T$ is the opposite of the vectorial sum of the lepton and the recoil energy: $\vec{\not{E}}_T = -(\vec{u}_T + \vec{E}^l_T)$. A non-zero magnitude for this vector can be found in events without neutrinos due to cracks in the calorimeters or mismeasurements. The recoil energy $\vec{u}_T$ has to be corrected for any underlying event energy that was deposited in the towers associated with the lepton. This contribution is estimated from the energy detected in calorimeter towers away from the lepton.

E. Jet detection

Jet reconstruction is the most commonly used tool to detect the presence of quarks or gluons in the event. The nature of the strong force governing the parton interactions makes it energetically favorable to pull $q\overline{q}$ pairs from the vacuum as the quark or the gluon fly away from the production point. These additional $q\overline{q}$ pairs recombine to form a collimated shower of lower-energy hadrons whose spatial distribution is highly correlated with the direction of the originating quarks and gluons. The ensemble of particles produced by this "hadronization process" is called a jet.

A jet is normally reconstructed with a fixed-cone clustering algorithm of radius $R = \sqrt{\Delta\eta^2 + \Delta\phi^2}$. The jet is seeded by the highest energy calorimeter tower in the event which is chosen as the axis of the cone. Any tower found in a cone of radius R is vectorially added to the jet, whose energy and direction are recursively calculated after any addition until no more towers are added. Typical cone sizes range from $R = 0.3$ to $R = 0.7$. Smaller or bigger cone sizes usually result in poorer energy resolution because of leakage of particles produced in the fragmentation or increasing contribution of energy from the underlying event. Also as R increases, the jets from two distinct original partons can merge resulting in lower detection efficiencies.

IV. EARLY STUDIES OF THE W BOSON AT HADRON COLLIDERS

The use of hadron colliders to investigate the weak interaction directly was first proposed in 1976, shortly after the first neutral current results provided a useful measurement of $\sin^2\theta_W$, and hence a strong indication that the W and Z masses were in the range of 50 to 100 GeV. The proposal to create a proton-antiproton collider was based on the necessity of using a single ring to contain both beams, as well as the desire to have valence antiquarks in order to produce the gauge bosons with the largest possible cross sections. The proposal to convert the CERN SPS into a proton-antiproton collider was approved in 1978, and first collisions at $\sqrt{s}$ =546 GeV were produced in 1981.

A. S$p\overline{p}$S experiments: UA1 and UA2

The production and decay of the charged boson $W \to l\nu$ was first observed by the two general-purpose experiments UA1 and UA2 in 1982 (Arnison *et al.*, 1983a; Banner *et al.*, 1983). The observation of the neutral boson $Z \to l^+l^-$ followed in early 1983 (Arnison *et al.*, 1983b; Bagnaia *et al.*, 1983). The analysis of these early data showed that:

- the masses of W and Z bosons are in the expected range based on the SM (Sirlin, 1980; Marciano and Sirlin, 1980; Llewellyn Smith and Wheater, 1981)
- the production properties are consistent with the Drell-Yan mechanism (Drell and Yan, 1970)
- the decay properties of W and Z bosons are consistent with the SM expectations (Weinberg, 1967).

The energy of the machine grew to $\sqrt{s}$ =630 GeV, and the data samples reached several hundred W bosons and several dozen Z bosons by the end of 1985. During this period, 0.7 pb^{-1} and 0.9 pb^{-1} of integrated luminosity were accumulated by the UA1 and UA2 experiments, respectively. These data samples allowed the first precision studies of electroweak interactions in hadron colliders. The production and decay properties of the W and Z bosons were measured (Arnison *et al.*, 1985, 1986; Albajar *et al.*, 1989; Appel *et al.*, 1986; Ansari *et al.*, 1987a). The SM parameters derived from the W and Z masses were found to be in good agreement with those obtained in deep inelastic neutrino interactions. The cross sections, the longitudinal and transverse momentum distributions and the characteristics of the rest of the event, including the associated production of high p_T jets, showed good agreement with the QCD improved Drell-Yan model expectations. There was no evidence for any exotic process leading to heavier intermediate vector bosons, heavy leptons or supersymmetric particles.

In the following 5 years, high luminosity CERN S$p\overline{p}$S runs with the improved antiproton source allowed the UA2 experiment (Alitti *et al.*, 1992a, 1992b) to collect an additional $\sim$ 14 pb^{-1} of data ($\sim$4000 W's).

B. CDF at the Tevatron Collider: 1985-1990

After the initial engineering run of the Tevatron collider in 1985, the CDF detector was commissioned and collected $\sim$ 25 nb^{-1} of integrated luminosity at $\sqrt{s}$ = 1800 GeV in 1987. The energy increase at the Tevatron collider resulted in a significant increase in the W production cross section and initiated a new era of precision studies of electroweak interactions at hadron colliders by delivering $\sim$ 4 pb^{-1} to the CDF detector during the 1988-89 period, corresponding to $\sim$2700 W candidates. Measurement of the W production and decay properties (Abe *et al.*, 1989, 1991a, 1991b, 1992a) and searches for heavier intermediate vector bosons (Abe *et al.*, 1991c) continued with no evidence of deviations from the SM predictions.

V. PROPERTIES OF THE W BOSON

In this section we discuss the measurements of the W mass, width and production cross-section, the lepton charge asymmetry in W decays, p_T^W and jets accompanying W production, and searches for additional charged gauge bosons, rare W decays and anomalous gauge couplings.

The recent Tevatron run was divided into three periods, usually denoted Run 1A (1992-93), Run 1B (1994-95) and Run 1C (1995-96). During these periods, the CDF and DO experiments have collected samples of over 200,000 W candidates each coming from $\sim$20 pb^{-1} in Run 1A, $\sim$90 pb^{-1} in Run 1B and $\sim$20 pb^{-1} in Run 1C.

CDF is able to trigger on and measure the momentum of electron and muon tracks in the central pseudorapidity region ($|\eta| < 1$) with good precision. Central electrons are required to have a track with a momentum comparable to the energy deposition in the calorimeter. The muons must be detected by a track in the central tracking chamber matching hits in either the central muon system, which covers the region $|\eta| < 0.6$, or by the central muon extension system, which extends the muon coverage to $|\eta| < 1$. Forward electrons ($1.1 < |\eta| < 2.4$) and muons ($1.9 < |\eta| < 2.5$) are also collected but without the requirement of a matching track. The W candidates are further required to have a neutrino by requiring significant $\not\!\!E_T$ in the event, typically $\not\!\!E_T > 25$ GeV. The CDF central electron and muon samples consist of $\sim$61,000 and $\sim$34,000 W candidates respectively. The combined forward rapidity electron and muon samples have $\sim$26,000 W candidates.

DO relies on its good calorimetry to measure the electron energy with good precision. By exploiting its forward coverage, DO measures both central ($|\eta| < 1$) and forward ($1.5 \, |\eta| < 2.5$) electrons. By requiring $E_T^e > 25$ GeV and $\not\!\!E_T > 25$ GeV, the DO central and forward rapidity electron samples consist of 49,000 and 19,000 W candidates respectively. About 11,000 $W \to \mu\nu$ candidates are identified by detecting muons in the muon system and requiring $\not\!\!E_T$ in the event.

A. Mass

Since the longitudinal component of the neutrino momentum $p_z(\nu)$ is unknown, one cannot reconstruct the $l\nu$ invariant mass for $W \to l\nu$ candidate events and must resort to other kinematic variables for the mass measurement.

The most common variable is the transverse mass (m_T), analogous to the invariant mass but computed using only the transverse components of the lepton momenta. The transverse mass is given by

$$\begin{aligned} m_T &= \sqrt{(E_T(l) + E_T(\nu))^2 - (\vec{p}_T(l) + \vec{p}_T(\nu))^2} \\ &= \sqrt{2p_T(l)p_T(\nu)\,(1 - \cos(\phi(l) - \phi(\nu)))} \quad . \end{aligned} \tag{22}$$

This variable has the advantage that its spectrum is relatively insensitive to the production dynamics of the W boson, the leading correction due to p_T^W being $\mathcal{O}((p_T^W/M_W)^2)$. The transverse mass is also insensitive to selection biases that prefer certain event topologies. However, it makes use of the inferred neutrino p_T and is therefore sensitive to the response of the detector to the recoil particles.

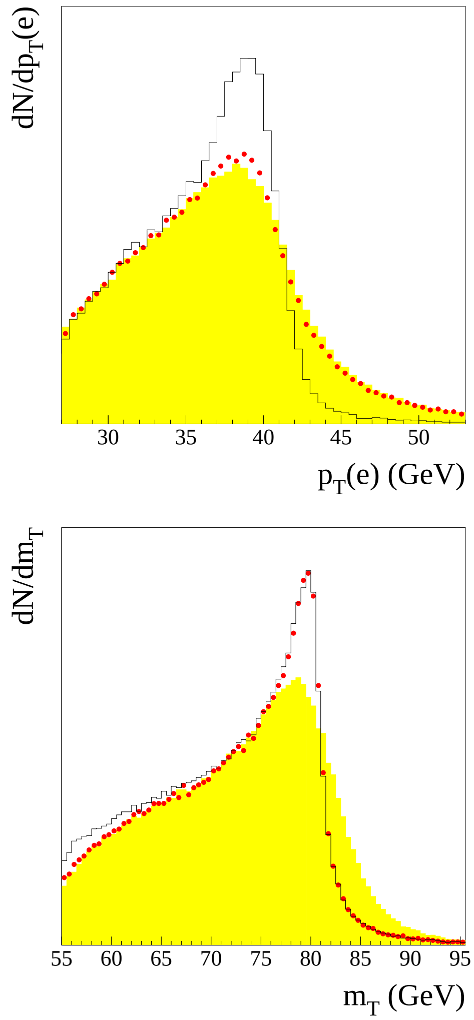

FIG. 8. The $p_T(e)$ (top) and m_T (bottom) spectra for W bosons with $p_T^W = 0$ (——), with the correct p_T^W distribution (•), and with detector resolutions (shaded).

The charged lepton p_T spectrum provides an alternative measurement of the W mass. Since the lepton p_T is bounded by the mass of the decaying W boson and the phase space peaks at 90° in its rest frame, the lepton p_T and m_T distributions have the characteristic jacobian shape (see Fig. 8). There are two effects that smear the jacobian edge of the p_T distribution at $M_W/2$ and the m_T distribution at M_W. Firstly, the finite W width causes the mass to be distributed according to the Breit-Wigner lineshape about the pole mass. Secondly, the lepton p_T is not invariant under transverse boosts of the W boson, receiving a correction to first order in $\vec{p}_T^W \cdot \hat{p}_T(l)$, where $\hat{p}_T(l)$ is the unit transverse vector in the lepton direction. Although it is measured with better resolution than m_T because it is insensitive to the recoil momentum measurement, it requires a better understanding of the W production dynamics than the m_T spectrum.

These effects are illustrated in Fig. 8, which show the effect of p_T^W and the detector resolutions on the shapes of the m_T and $p_T(e)$ spectra. We observe that the shape of the m_T spectrum is dominated by detector resolutions and the shape of the $p_T(e)$ spectrum by p_T^W.

A third variable which contains W mass information is the neutrino p_T. The shape of the neutrino p_T spectrum is sensitive to both the W production dynamics and the recoil momentum measurement. By performing the measurement using all three spectra, one can perform powerful cross checks and obtain results with complementary systematics.

1. Mass measurement strategy

For recent measurements (Alitti *et al.*, 1990; Abe *et al.*, 1990b; 1991a, 1995e; Abachi *et al.*, 1996b; Abbott *et al.*, 1998a, 1998d, 2000a, 2000c) the transverse mass of the lepton-neutrino system was used. DO performs a maximum likelihood fit to the m_T, $p_T(e)$ and $p_T(\nu)$ spectra while CDF uses the mass measurement from $p_T(l)$ and $p_T(\nu)$ as a cross-check. Since these distributions, including all the experimental effects, cannot be computed analytically, one needs a fast parametric Monte Carlo simulation program that can predict the shape of the spectra as a function of the W mass with high statistical precision.

Using the data collected during Run 1B, CDF performs the W mass measurement with central electrons and muons. DO exploits its forward tracking coverage to perform the measurement using both central and forward electrons. The DO muon momentum measurement is not sufficiently precise to measure the W mass effectively.

CDF and DO also published W mass results with data collected during Run 1A. CDF performed its first W mass measurement using ≈ 4 pb^{-1} of data collected during the 1988-1989 Tevatron run, when it was the only detector installed along the Tevatron ring.

2. Electron response and resolution

CDF and DO use different strategies to measure the W mass with electrons, because CDF has a very stable and linear magnetic tracker, while DO has a very stable and linear EM calorimeter.

CDF derives the absolute energy scale from the momentum scale calibration of the central tracking chamber

(CTC). Therefore the CTC must be understood very well and its calibration proceeds as follows. First the electron tracks in $W \to e\nu$ decays are used to align the CTC. Any first-order correction to the track curvature causes a difference in the momentum measurement of electrons and positrons because they bend in opposite directions. On the other hand, the calorimeter energy measurement is indifferent to the charge. Thus the calorimeter energy measurement of electrons and positrons is used to measure and correct for curvature errors in the CTC.

For the typical momentum of tracks from W decay, the calorimeter resolution is better than the track resolution. Therefore the calorimeter E measurement is used to obtain the final electron four-momentum for the W mass fit. The track momentum calibration is transferred to the calorimeter using the E/p ratio measured in W events. Uniformity corrections are made to the calorimeter to equalize the individual tower responses, remove the response variation within the tower, and remove the time dependence of the response.

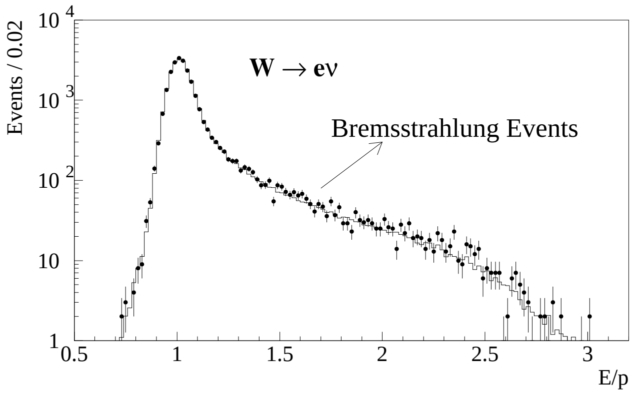

FIG. 9. The E/p spectrum for CDF $W \to e\nu$ candidates (•), compared with the simulation (−).

The effects of detector material on track parameters is studied using conversion photons. The distribution of the photon conversion radius, after correcting for radius-dependent trigger and conversion-finding efficiency, maps out the radial distribution of the material in radiation lengths. The absolute amount of material is referenced to the known thickness of the CTC inner wall.

The effects of this material on electron track parameters is cross-checked by studying the ratio of electron calorimeter energy E to the measured track momentum p (E/p ratio). The bremsstrahlung photon is merged with the track in the calorimeter, hence E is not very sensitive to bremsstrahlung energy loss. The E/p ratio is thus a measure of the effect of bremsstrahlung on p. The E/p ratio measured in W decays is compared with the prediction of a simulation based on the material distribution extracted from the conversion electron analysis. The comparison shows consistency between the two methods (see Fig. 9).

The $J/\psi \to \mu\mu$ invariant mass is used to set the overall momentum scale of the tracker. Residual corrections are made based on the polar angle dependence of the measured J/ψ mass, and ϕ dependence of the E/p ratio in W events. Further cross-checks are made with the $\Upsilon \to \mu\mu$ invariant mass (see Fig. 10). Finally, the linearity of the tracker is checked by studying the dependence of the measured J/ψ and Υ masses on the curvature of the tracks.

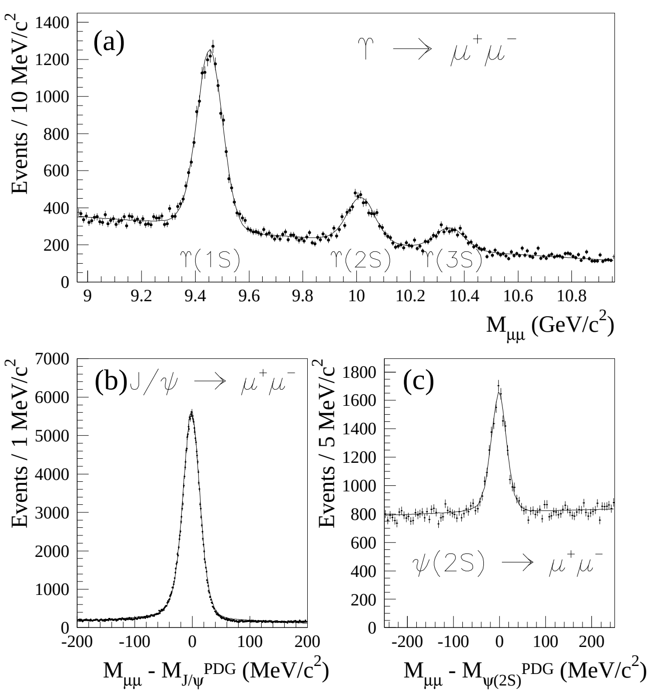

FIG. 10. The ψ and Υ mass fits (−) to the CDF data (•).

This extensive and detailed calibration procedure provides a statistically precise calibration of the tracker and the calorimeter. However, an irreconcilable discrepancy was found between the measured $Z \to e^+e^-$ invariant mass and the precisely measured Z mass measured at LEP. Various possible sources of this discrepancy were investigated, but an explanation has not been uncovered. Therefore the most reliable W mass measurement is quoted by scaling to the measured Z mass, albeit with a larger statistical error (due to Z event statistics) and a potential non-linearity uncertainty.

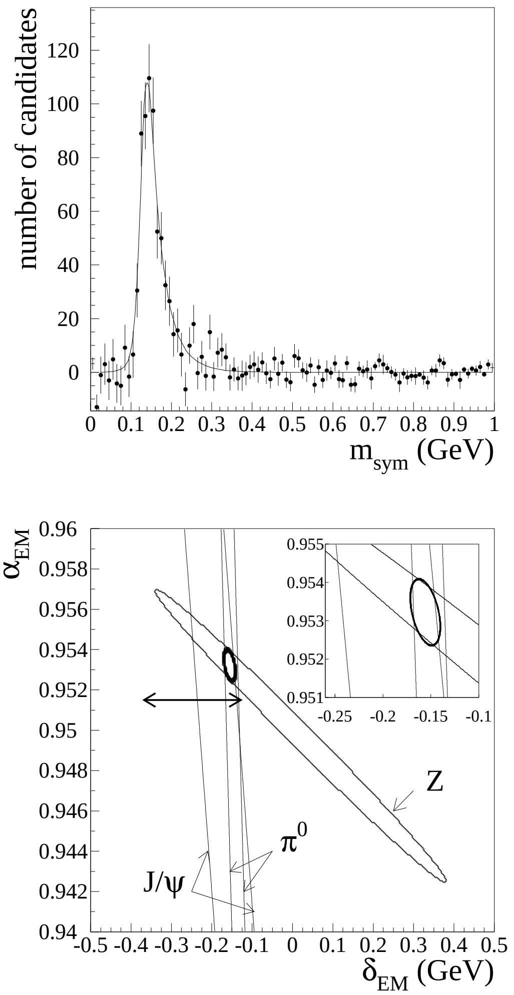

FIG. 11. The π^0 symmetric mass fit (top) and the combined $\alpha_{EM} - \delta_{EM}$ constraint (bottom) for the central calorimeter from DO.

The absolute energy scale calibration at DO is performed directly using known resonance masses. The linearity of the central and forward calorimeters was measured extensively in beam tests. The sampling fractions for the calorimeter layers were extracted from test-beam data. The calorimeter response measured in beam tests is consistent with the linear parameterization at high energy, $E_{meas} = \alpha_{EM} \cdot p_{true} + \delta_{EM}$ with indication of deviation from the straight-line response at low energy.

The EM offset parameter δ_{EM} is measured using low mass resonances, π^0 and $J/\psi \to ee$, which are sensitive to δ_{EM}. The π^0 is reconstructed by identifying candidates in which both photons convert. In the absence of a central magnetic field, the tracks from the conversion electron-positron pair overlap and are detected as a single doubly-ionizing track, which gives the direction of the converted photon. The energy of each photon cannot be measured separately because the two clusters merge in the calorimeter. By splitting the total π^0 energy equally between the two photons, a quantity called symmetric mass can be reconstructed. The symmetric mass distribution is simulated based on the knowledge of the π^0 momentum spectrum and the calorimeter energy response. The latter is constrained by comparing the measured and simulated symmetric mass distributions (see Fig. 11).

The EM offset parameter can also be measured *in situ* using $Z \to e^+e^-$ decays. The electrons from Z decays are not monoenergetic and therefore one can make use of their energy spread to constrain δ_{EM}. When both electrons are in the same calorimeter, one can write $m_{ee} = \alpha_{EM} \cdot M_Z + f_Z \cdot \delta_{EM}$ for $\delta_{EM} \ll E(e_1) + E(e_2)$. f_Z is a kinematic function related to the boost of the Z, and is given by $f_Z = [E(e_1) + E(e_2)](1 - \cos\omega)/m(ee)$, where ω is the opening angle between the two electrons. A similar expression can be derived when one electron is central and one is forward. Using this relation, DO extracts a joint constraint on α_{EM} and δ_{EM} (see Fig. 11). The final δ_{EM} for the central calorimeter (CC) is extracted from a combined analysis of the Z, J/ψ and π^0 information. The δ_{EM} for the end calorimeter (EC) is measured using Z data alone.

The EM offset measurement from the low mass resonances is sensitive to the deviation of the calorimeter response from the straight-line ansatz. This low energy non-linearity is constrained by the test-beam data, and determines the dominant systematic error on the low-mass resonance determination of the EM offset.

After correcting the data for the measured CC and EC offsets, DO determines α_{EM} so that the position of the Z peak predicted by the Monte Carlo agrees with the data, by performing a maximum likelihood fit to the $m(ee)$ spectrum (see Fig. 12). Since the measured W mass is directly proportional to the energy scale parameter α_{EM}, DO in fact measures the ratio of W and Z masses.

The functional form of the electron energy resolution is given by

$$\left(\frac{\sigma_{\rm E}}{E}\right)^2 = C^2 + \left(\frac{S}{\sqrt{E_T}}\right)^2 + \left(\frac{N}{E}\right)^2 . \qquad (23)$$

CDF and DO take the intrinsic resolution of the calorimeter, which is given by the sampling term S, from the test beam measurements. The noise term N is represented by the width of the electron underlying event energy distribution, which is measured from the data and used in the simulation. The constant term C is measured from the Z line shape of the data, since the true Z width is known well from LEP measurements.

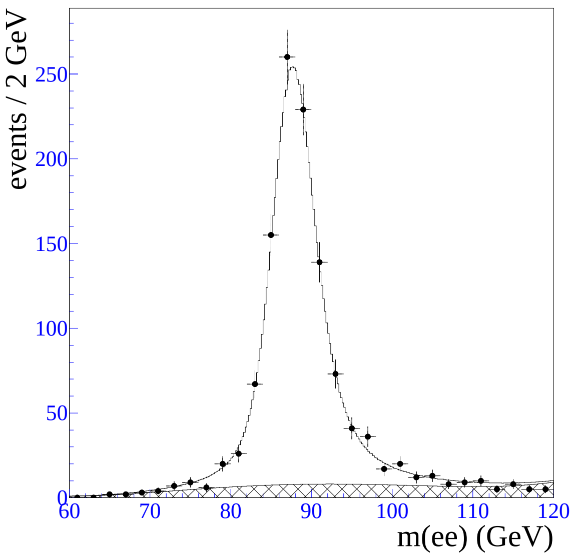

FIG. 12. The DØ dielectron mass spectrum from the CC/EC Z sample. The superimposed curve shows the maximum likelihood fit and the shaded region the fitted background.

3. Muon response and resolution

CDF uses the $Z \to \mu^+\mu^-$ events to set the tracker momentum scale for muons. All of the CTC alignment, calibration and material studies are performed and used jointly for the electron and muon channel analyses. Samples of $J/\psi \to \mu\mu$ and $\Upsilon \to \mu\mu$ events are used to check the momentum scale and possible non-linearity. The momentum of each muon is corrected for energy loss in the material traversed by the muon. The high statistics Υ and ψ samples were also used to check for possible time dependence in the momentum scale; none was found. The final momentum scale was set with the $Z \to \mu^+\mu^-$ events alone in order to have a procedure consistent with the electron channel analysis.

CDF determines the muon momentum resolution from the W and Z data. The wire hit patterns from W data are used to determine the track covariance matrix, which is then used to smear the muon track in the simulation. The covariance matrix is scaled by an overall resolution parameter. The resolution parameter is then extracted by fitting the $Z \to \mu^+\mu^-$ data lineshape with Monte Carlo templates. The momentum scale and resolution measurements are largely uncorrelated.

4. Recoil response and resolution

The detector response and resolution for particles recoiling against a W should be the same as for particles recoiling against a Z boson. For $Z \to l^+l^-$ events, one can measure p_T^Z using the p_T of the l^+l^- final state ($p_T(l^+l^-)$), and using the recoil momentum u_T (in the same way as for $W \to l\nu$ events). By comparing $p_T(l^+l^-)$ and u_T, CDF and DØ calibrate the recoil response relative to the electron response.

The widths of the p_T balance distributions in two orthogonal transverse directions are sensitive to the recoil resolution. The recoil resolution receives contributions from the "hard" recoil of particles causing the boson p_T, and the "soft" component due to the underlying event. The former component is measured by studying the p_T dependence of the width of the p_T balance in $Z \to l^+l^-$ events. The latter is independent of the boson p_T and is derived from the measured p_T imbalance in minimum bias events. The parameters in the overall recoil resolution parameterization are then measured by fitting the $Z \to l^+l^-$ data. Since the W mass analysis samples are restricted to low measured boson p_T ($p_T(W) < 15$ GeV for DØ and $p_T(W) < 20$ GeV for CDF), the resolution on the "soft" component of the hadronic activity dominates the total recoil resolution.

As described above, the detector response model in both CDF and DØ W mass analyses are tuned largely on the $Z \to l^+l^-$ collider data. As a cross-check, various distributions measured in the W data are compared with the predictions of the Monte Carlo simulation. These checks provide important confirmation that the detector response is well understood.

5. Production and decay dynamics

The production and decay dynamics of the W influence the kinematics of the decay leptons, thus affecting the fitted value of the W mass. The relevant aspects of the W production and decay dynamics are the transverse momentum and longitudinal boost distributions, the parton luminosity, the decay angular distribution, and QED radiative effects.

Both CDF and DØ use the Z events to understand the p_T^W distribution, since the production dynamics are very similar. While the recoil resolution is too poor to enable the direct measurement of the true p_T^W at low p_T, the decay leptons from the Z boson can be measured well and the true p_T^Z can be inferred from them. CDF uses an empirical fit to the p_T^Z distribution from the leptons as the input to the Monte Carlo simulation. The p_T^W distribution is derived from this by using the calculated ratio of p_T^W and p_T^Z distributions. The calculation is based on the model described in Sec. II.A with perturbative, non-perturbative and resummed components of the boson p_T spectra. DØ uses the same calculation to predict the p_T^W and p_T^Z spectra, and tunes the parameters in the model to fit the Z data. In either technique, the statistics of the Z data dominate the uncertainty in the predicted p_T^W spectrum.

In principle, if the acceptance for the W decays were complete, the transverse mass distribution or the lepton

p_T distributions would be independent of the W rapidity. However, cuts on the lepton angle in the laboratory frame cause the observed distributions of the transverse momenta to depend on the W rapidity. Hence a constraint on the W rapidity distribution is useful in limiting the production model uncertainty on the W mass.

CDF has used the lepton charge asymmetry from W decays to constrain PDFs (see next section), which in turn control the W rapidity distribution. The DO measurement is less sensitive to PDFs since the combined central and forward electron measurements imply a more complete rapidity coverage. DO has also checked that the rapidity spectrum of the decay electron, which is correlated with the W rapidity, agrees with the Monte Carlo prediction when corrected with the rapidity-dependent efficiency and background.

CDF and DO use the calculation of Mirkes (1997) described in Sec. II.A to predict the W decay angular distribution. DO has made a preliminary measurement of the α_2 parameter as a function of p_T^W. Though statistically limited, the measurement is consistent with the calculation of Mirkes (1997).

Both experiments use the Berends and Kleiss (1985) calculation to simulate QED radiative decays of the W boson (see Sec. II.C). The Monte Carlo simulation includes the detector response to the radiated photon, including the merging of collinear photons with the electron in the calorimeter.

6. Backgrounds

Backgrounds in the W candidate sample arise from physics sources which have an indistinguishable final state, and detector-related causes such as misidentification or acceptance losses. In the former case, the dominant background is $W \to \tau\nu \to l\nu\overline{\nu}\nu$, which is kinematically suppressed because of the significantly lower lepton p_T. This source of background in included in the Monte Carlo simulation by generating the decay with the appropriate branching ratio. This background fraction is approximately 1%. Other sources of background with similar final states, such as $Z \to \tau^+\tau^-$, WW and $t\bar{t}$ are negligible.

Detector-related backgrounds arise from QCD jet events where a jet mimics a lepton and there is sufficient energy mismeasurement to produce significant $\not{E}_T$, from $Z \to l^+l^-$ events where the second lepton is not detected, and from cosmic rays. Both experiments extract the shape of the "QCD" background in the signal sample by inverting the lepton identification cuts, thus rejecting true leptons and selecting a sub-sample of the misidentified leptons. The normalization of the background is obtained by applying the same lepton selection and anti-lepton selection cuts to a predominantly QCD jet sample. CDF uses an inclusive sample with low m_T, while DO uses a similar sample with low $\not{E}_T$ (see Fig. 13). The QCD background fraction in the DO central and forward electron samples are 1.6% and 3.6% respectively. In the CDF electron and muon W samples this background contributes about 0.4% within the fitting window.

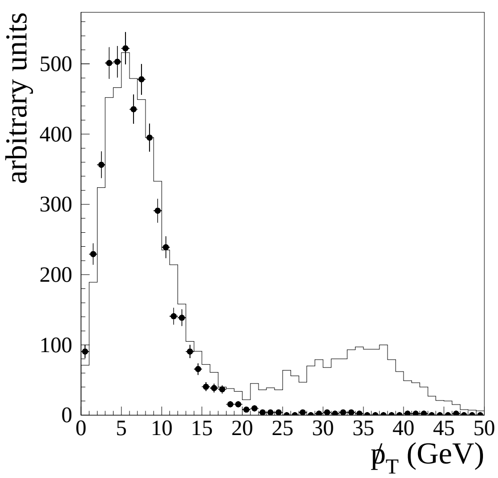

FIG. 13. The $\not{E}_T$ spectra of a sample of events from DO passing electron identification cuts ($-$) and a sample of events failing the cuts ($\bullet$).

Monte Carlo predictions are used to estimate the background from $Z \to l^+l^-$ with a missed lepton. This source contributes less than 0.5% in the DO samples and the CDF electron sample, and contributes 3.6% in the CDF muon sample due to a muon escaping the central tracker at small polar angles. Cosmic rays contribute 0.1% to the CDF muon sample, most of them having been removed by the rejection of back-to-back tracks and an impact parameter cut.

7. Mass fit results and uncertainties

CDF and DO use a binned maximum likelihood fit to extract the W mass. Using the fast Monte Carlo program, the m_T, $p_T(l)$ and $p_T(\nu)$ spectra are computed for a range of hypothesized values of the W mass. When fitting the data, the background contributions are added with the measured shapes and normalizations. The Monte Carlo spectra are normalized within the fit region and interpreted as probability density functions in order to compute the likelihood $L(m) = \prod_{i=1}^{N} p_i^{n_i}(m)$, where $p_i(m)$ is the probability density for bin i, assuming $M_W = m$, and n_i is the number of data entries in bin i. The product runs over all N bins inside the fit region. Both experiments fit $-\ln[L(m)]$ with a quadratic function of m. The value of m at which the function assumes its minimum is the fitted value of the W mass and the 68% confidence level interval is the interval in m for which $-\ln[L(m)]$ is within half a unit of its minimum. The fits to the Run 1B data are shown in Fig. 14 and 15. Table I summarizes the results.

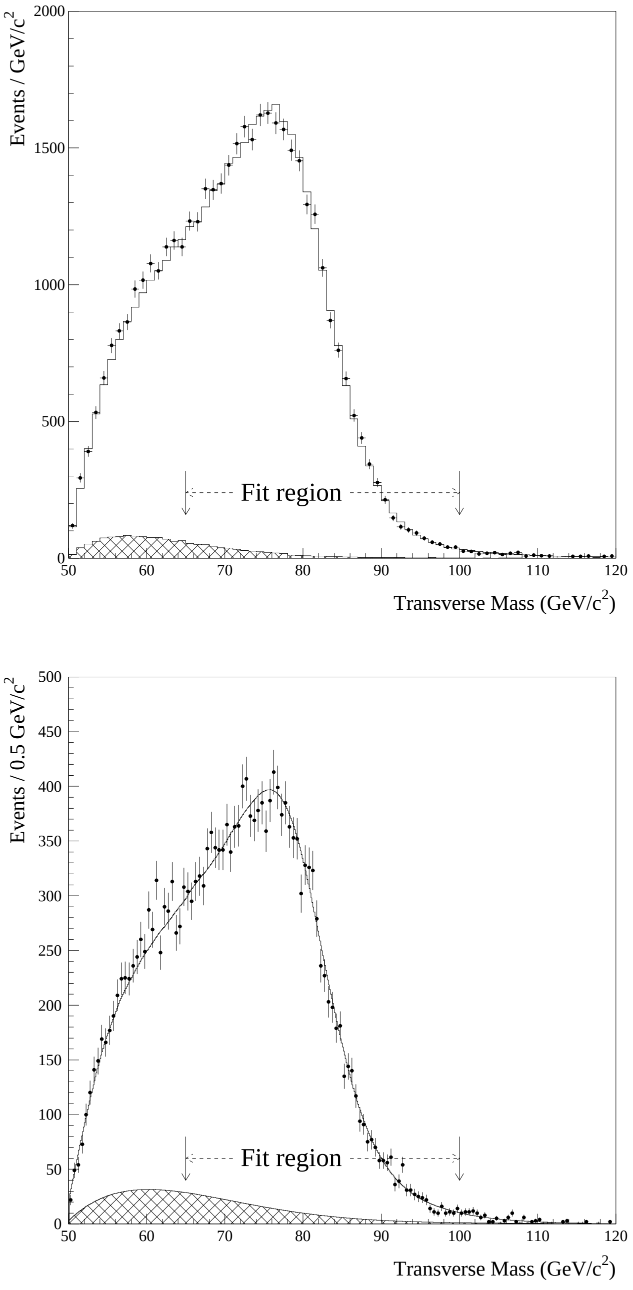

FIG. 14. The W transverse mass fits (–) to the CDF candidate events (•) and the expected backgrounds (hatched). The top plot shows the $W \to e\nu$ data and the bottom plot shows the $W \to \mu\nu$ data.

Extensive consistency checks are performed, including χ^2 and Kolmogorov-Smirnov probability tests between the data and the best-fit Monte Carlo spectra, deviations in the signed χ distributions, and stability of the fit results under changes in the fitting region. The samples are split into subsamples in bins of p_T^W and lepton p_T and the corresponding best fit Monte Carlo distributions are compared for consistency. DO also checks the variation of the fitted W mass when the data are binned in the azimuthal angle of the electron, the azimuthal angle of the recoil, instantaneous luminosity, chronological time, and when the fiducial cut on the pseudorapidity of the electron is varied. The stability of the measured mass under all these cross-checks gives confidence in the results.

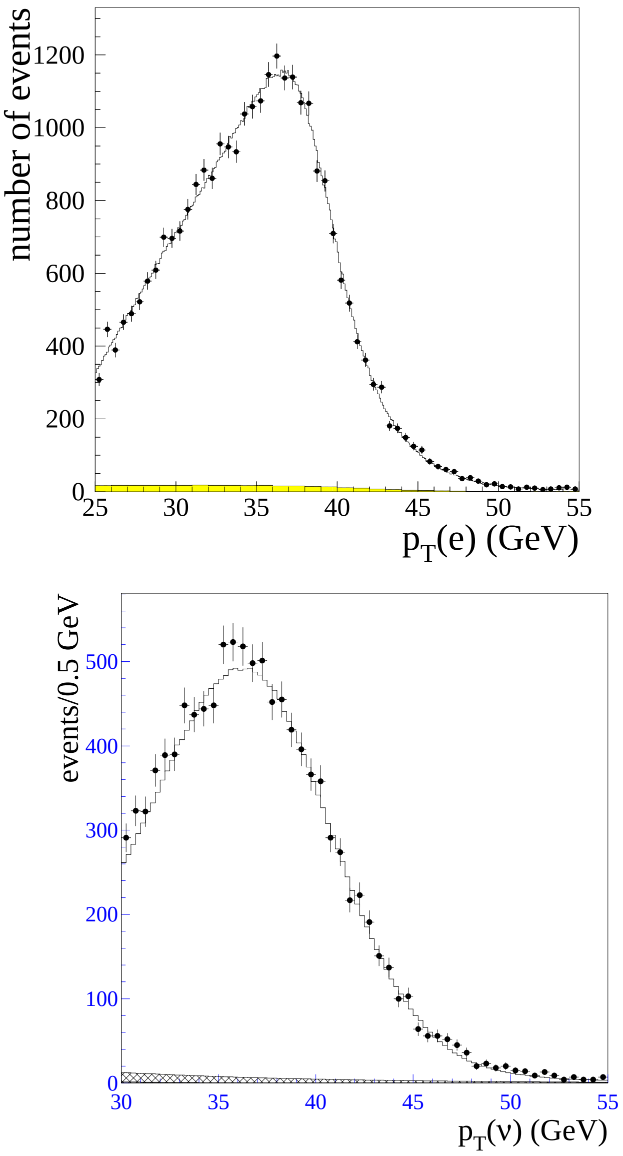

FIG. 15. The W mass fits (–) to the DO data (•) and expected backgrounds (shaded): the CC $p_T(e)$ spectrum (top) and the EC $p_T(\nu)$ spectrum (bottom).

As a consistency check, DO also fits the transverse mass distribution of the $Z \to e^+e^-$ events, reconstructed using each electron and the recoil. The measured energy of the second electron is ignored, both in the data and in the Monte Carlo used to obtain the templates. The fits are good and the fitted masses are consistent with the input Z mass.

CDF performs a simultaneous fit for the W mass and width near the jacobian edge. The W width obtained is consistent with the SM value, and fitted mass is consistent with the result from the one-dimensional fit. This gives confidence that the detector response which affects the observed jacobian edge has been modelled correctly in the simulation.

Systematic uncertainties on the fitted W masses are estimated using the Monte Carlo simulation. The various parameters defining the production and decay model, the detector response to the lepton and the hadronic recoil, and the background shapes and normalizations are varied by $\pm 1\sigma$ and the effect propagated to the W mass. CDF keeps track of correlated errors between the electron and muon measurements, while DO keeps track of the correlations between the central and forward electron analyses and the correlations between the m_T, $p_T(e)$ and $p_T(\nu)$ fits in both analyses. Correlations with analyses based on previous Run 1A data sets are also noted.

Tables II and III show a summary of the systematics on the CDF and DO results from Run 1B. DO has combined the six measurements (central and forward electron samples and m_T, $p_T(e)$ and $p_T(\nu)$ fits) using a sophisticated error analysis taking into account all statistical and systematic correlations. The combined Run 1B DO measurement is $M_W = 80.498 \pm 0.095$ GeV. The χ^2/dof is 5.1/5, with a probability of 41%. The consistency of the six results indicates that the ingredients of the Monte Carlo model and their uncertainties are understood. The CDF Run 1B combined electron and muon channel result is $M_W = 80.470 \pm 0.089$ GeV. By including the measurements from Run 1A, the Run 1 masses become:

$$\begin{aligned} M_W^{DO} &= 80.482 \pm 0.091 \text{ GeV} \\ M_W^{CDF} &= 80.433 \pm 0.079 \text{ GeV} \quad . \end{aligned} \tag{24}$$

A global fit to all electroweak measurements excluding the direct W mass measurements predicts $M_W = 80.367 \pm 0.029$ GeV (LEP Collaborations, 2000a). Figure 16 gives a summary of the most recent direct W mass measurements.

In Fig. 17 we compare the measured W and top quark masses (Abbott *et al.* 1998c, 1999a; Abe *et al.* 1999a) from CDF and DO with the the values predicted by the SM for a range of Higgs mass values (Degrassi *et al.*, 1998; Degrassi, Gambino, and Sirlin, 1997). Also shown is the prediction (Chankowski *et al.*, 1994; Garcia and Sola, 1994; Dabelstein, Hollik, and Mosle, 1995; Pierce *et al.*, 1997) for a model involving supersymmetric particles assuming the chargino, Higgs, and left-handed selectron masses are greater than 90 GeV. The measured values are in agreement with the prediction of the SM, and weakly favor a light standard model Higgs.

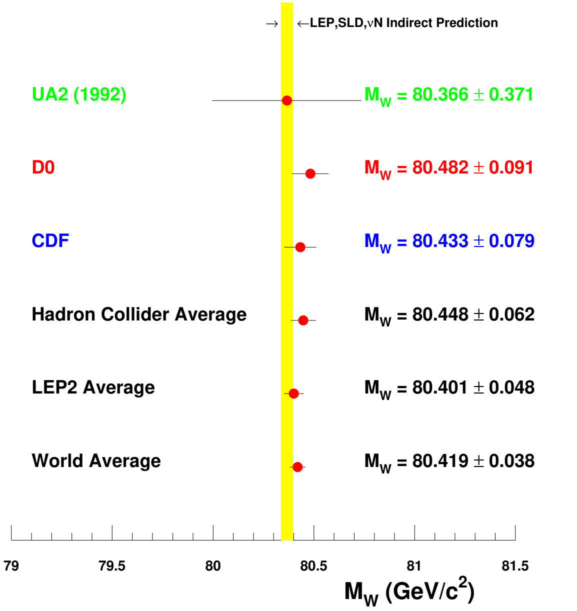

FIG. 16. A comparison of recent direct measurements of the W mass. The shaded region indicates the predicted W mass value from global fits to other electroweak measurements (LEP Collaborations, 2000a).

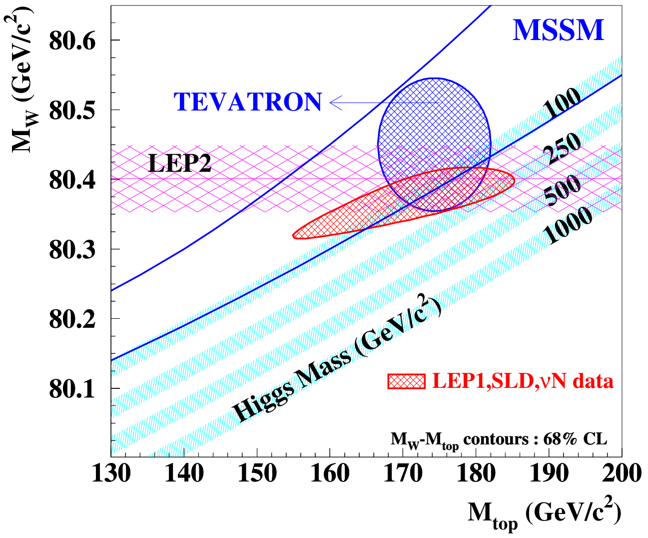

FIG. 17. A comparison of the W and top quark mass measurements with the SM predictions for different Higgs masses (Degrassi *et al.* 1998; Degrassi, Gambino, and Sirlin, 1997). The width of the bands for each Higgs mass value indicates the uncertainty due to the error in $\alpha(M_Z^2)$. Also shown is the direct W mass measurement from the LEPII experiments and the indirect limits from LEP1, SLD and neutrino experiments. The area between the two solid lines is the range allowed by the MSSM (Chankowski *et al.* 1994; Garcia and Sola, 1994; Dabelstein, Hollik, and Mosle, 1995; and Pierce *et al.* 1997).

B. Width

The W width can be measured directly by analysing the W lineshape, which is given by the Breit-Wigner distribution (see Eqn. 13). In a hadron collider, the mass dependence of this cross section is modified by the parton luminosity, which is the $q\bar{q}$ flux with the pair invariant mass of $\sqrt{\hat{s}}$. The parton luminosity can be calculated by convoluting the parton distribution functions (f_q and $f_{\bar{q}}$ in Eqn. 12) for the colliding hadrons.

In principle, the entire high-m_T half of the Jacobian edge contains information on Γ_W. However, the distribution falls rapidly close to the jacobian peak and therefore is sensitive to the detector resolution, particularly the hadronic recoil resolution used to reconstruct $p_T(\nu)$. But away from the jacobian peak, the Breit-Wigner distribution falls slowly compared to the resolution and is much less sensitive to resolution smearing. CDF performs an analysis of the m_T lineshape in the range $100 < m_T < 200$ GeV to extract Γ_W, where the lower window limit is chosen to optimize the sensitivity considering both statistical and systematic uncertainties.

1. Direct Γ_W Measurement

CDF has performed the direct measurement of the total W width in the electron decay channel using Run 1A data (Abe *et al.*, 1995a) and in both electron and muon decay channels using Run 1B data (Abe *et al.*, 2000b). The analysis technique and procedure is similar to the W mass measurement described in Sec. V.A. The simulation produces m_T spectra for Γ_W values between 1.0 GeV and 3.0 GeV in 50 MeV steps. Each spectrum is normalized to the background-subtracted data in the region $m_T < 200$ GeV, and backgrounds with the measured shapes and normalizations are added to the predicted spectra. A binned likelihood fit in 1 GeV bins over the $100 < m_T < 200$ GeV window yields $\Gamma_W = 2.175 \pm 0.125$ (stat) GeV for the electron channel and $\Gamma_W = 1.780 \pm 0.195$ (stat) GeV for the muon channel. Figure 18 shows the m_T distributions with the best-fit Monte Carlo templates and the backgrounds.

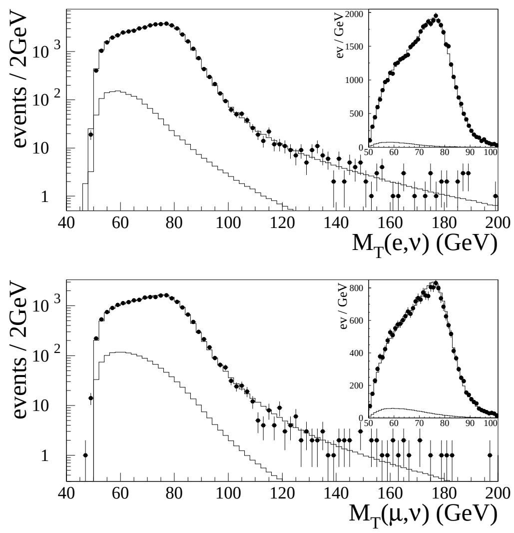

FIG. 18. CDF transverse mass spectra (filled circles) for $W \to e\nu$ (upper) and $W \to \mu\nu$ (lower) data, with best Monte Carlo fits superimposed as a solid curve. The lower curve in each plot shows the sum of the estimated backgrounds. Each inset shows the 50-100 GeV region on a linear scale.

Sources of systematic uncertainty that alter the shape of the m_T distribution are the electron and muon energy scales, the non-linearity of the calorimeter affecting the electron E_T, the recoil model, the p_T^W spectrum, the PDFs, QED radiative corrections, the W mass and the backgrounds. The systematic uncertainties for the measurements from the Run 1B data are summarized in Table IV. The combined $e + \mu$ result is $\Gamma_W = 2.04 \pm 0.11$ (stat) ± 0.09 (syst) GeV. The result is in good agreement with the SM prediction $\Gamma_W = 2.093 \pm 0.002$ (Particle Data Book, 1998) and puts an upper limit on the W partial width into new decay modes.

C. Cross Section

As we saw in Sec. I.B, the production cross sections of W and Z bosons provide insight into the proton's internal structure and the W and Z couplings to quarks. The largest single source of uncertainty in the measurement of the inclusive W and Z cross sections is the integrated luminosity used for the absolute normalization. By carefully designing the analysis, the luminosity normalization can be completely cancelled in $\sigma \cdot B$ ratio of the W to Z bosons, along with certain other sources of systematics, thus making the measurement of R in Eqn. 9 much more precise than the individual $\sigma \cdot B$ measurements. R is used to derive an indirect measurement of Γ_W, according to the method discussed in Sec. I.A, exploiting the fact that also on the theoretical side the calculation of the inclusive cross section ratio $\frac{\sigma_W}{\sigma_Z}$ is less sensitive to PDFs and QCD evolution. Similar considerations apply to the measurement of $\tau - e$ universality using the ratio of $\sigma_W \cdot B$ in the τ and e channels (see Eqn. 11).

CDF and DO have published measurements of $\sigma \cdot B$ for the electron and muon decay channels of W and Z bosons, and Γ_W extracted from R. DO published both electron and muon channel measurements from the Run 1A data (Abachi *et al.*, 1995c, Abbott *et al.*, 1999a) and the electron channel measurement from the Run 1B data (Abbott *et al.*, 2000b). CDF has published these measurements in the electron channel from the Run 1A data only (Abe *et al.*, 1995g, 1996b). The most recent τ channel measurement was performed by DO from Run 1B data (Abbott *et al.*, 2000e) using a special τ trigger.

1. Electron measurement

Both central and forward electrons are used. CDF requires the W electron to be central and at least one of the two Z electrons to be central. The second Z electron is allowed to be forward in order to increase the Z acceptance, and so that the second electron's rapidity distribution follows that of the neutrino in the W decay. This causes the uncertainty in the acceptance for the W and Z bosons to correlate strongly and hence cancel in the cross section ratio. DO uses both central and forward electrons for the W decay, and allows either Z electron to be central or forward.

Similar reasoning guides the electron identification requirements. The W electron is required to satisfy electromagnetic cluster cuts and is required to have a matching track associated with the cluster. One of the Z electrons is required to satisfy the same criteria, while the second electron has much looser requirements. The latter technique not only increases the Z identification efficiency (Z statistics are a limitation while W statistics are not), but also causes the second Z electron to emulate the W neutrino more closely. This allows further cancellation of efficiency-related systematics in the cross section ratio.

Detector acceptances are estimated using a Monte Carlo program similar to the one used for the direct W mass and width measurements. The boson mass, rapidity and p_T distributions are generated similarly, and the detector geometry, response and resolution to the lepton and the hadronic recoil are parametrized and modelled in the simulation. QED radiative effects are also simulated. The detector simulation is tuned on W, Z and minimum bias data using the techniques described earlier for the W mass analyses.

Electron identification efficiencies are measured using the $Z \to e^+e^-$ data. Tight cuts are used to identify one electron, and the invariant mass reconstructed with a second loosely identified electromagnetic cluster is required to be in the Z peak region. A fairly pure $Z \to e^+e^-$ sample can be identified in this way. The second electromagnetic cluster provides an unbiased sample with which to measure the identification cut efficiencies.

This technique assumes that the cut efficiencies for the two electrons are uncorrelated. DO has checked for such correlations in the calorimeter-based cuts by using a GEANT-based simulation. The impact of such a correlated bias is found to be small compared to the uncertainty on the efficiency, and is neglected. The track-based cuts are checked using the data. The tracking efficiency is found to be 1.7% lower than what one would get assuming no correlations. The effect of this correlation cancels in the ratio of cross sections.

The $W \to e\nu$ backgrounds are estimated using the same techniques as described in the W mass analysis section. The $Z \to e^+e^-$ background fraction is estimated using the sidebands of the Z peak. The background shape is determined from data selected similarly to the signal sample, but passing anti-electron cuts. One then fits for the background fraction by fitting the $Z \to e^+e^-$ mass distribution with a linear combination of the background shape and simulated signal shape.

The measurement of the absolute luminosity is very important for the measurement of the inclusive W and Z cross sections. The luminosity is measured from the rate in scintillator counters close to the beam, and correcting for the counter efficiency and the acceptances for single diffractive, double diffractive and non-diffractive components of the total $p\bar{p}$ cross section. CDF and DO differ in their luminosity calculation in that CDF uses its own measurement of the inelastic $p\bar{p}$ cross section, while DO uses the "world average" of the results from CDF, E710 and E811. Consequently, CDF and DO cross sections are *ab initio* different, and care must be taken in comparing and combining their results and in comparing them to other hard-scattering cross sections.

DO has also measured the $W \to e\nu$ cross section at center-of-mass energy $\sqrt{s} = 630$ GeV, using data collected during Run 1C. Since there were insufficient $Z \to e^+e^-$ events to re-measure efficiencies, the efficiency measurements made at $\sqrt{s} = 1800$ GeV were extrapolated as a function of the extraneous energy density in the event. Background estimates were also extrapolated by scaling the estimates from $\sqrt{s} = 1800$ GeV data by the ratio of signal and background process cross sections. The result for 630 GeV is $\sigma_W \cdot B(W \to e\nu) = 658 \pm 58(\mathrm{stat}) \pm 34(\mathrm{syst})$ pb.

Table V shows the results and uncertainty contributions for the CDF and DO measurements of the cross sections. Table VI shows the same for the measurement of the cross section ratio R. Consistency checks are performed by measuring the cross section separately in each cryostat, and with subsamples binned in instantanous luminosity. Further checks are performed by measuring the cross sections and the cross section ratio with different kinematic cuts. Raising the kinematic cuts on the

p_T of the leptons reduces the acceptance but also reduces the backgrounds. Since the acceptance corrections and backgrounds for the W and Z samples are different, the stability of the measurements with variation in the kinematic cuts gives confidence that these corrections are well-understood.

2. Muon measurement

DO has published measurements of the inclusive $W \to \mu\nu$ and $Z \to \mu^+\mu^-$ cross sections and their ratio R from Run 1A using central muons. Candidate muon tracks must be confirmed by the presence of energy in the calorimeter along the muon trajectory. Typically a muon deposits ~ 3 GeV; at least 1 GeV is required. To obtain a reliable momentum measurement, the minimal integral of the magnetic field in the toroidal magnet along the muon track is required to be greater than 2 Tm. This requirement also eliminates regions of reduced calorimeter thickness (about 9 interaction lengths as compared to the typical 13-18 interaction lengths), and hence reduces punchthrough background. DO has a compact inner tracker and gains from reduced π and K decays to muons in flight compared to CDF. Cosmic ray background is reduced by requiring small impact parameters of the muon track relative to the interaction vertex, and correct drift time relative to the beam crossing. Muons from W and Z decay are expected to be isolated in energy compared to muons associated with jets, such as those produced from heavy quark decay. The latter are rejected by requiring the calorimeter energy along the muon track to not exceed the expected energy loss by more than 3σ, and by requiring that the calorimeter energy surrounding the muon in an $\eta\phi$ cone of radius 0.6 (isolation energy) be less than 6 GeV.

The W decay muon is required to satisfy all these criteria, as is one of the Z decay muons. The other Z muon is only required to deposit at least 1 GeV in the calorimeter. The efficiency of reconstructing muon tracks in the proportional drift tubes is measured by visually scanning event displays with very loose trigger requirements and no offline reconstruction requirements. Further identification efficiencies are measured from $Z \to \mu^+\mu^-$ events by making stringent cuts on one muon and using the other muon to measure the efficiency. The muon hardware trigger efficiency is determined from jet triggers containing a muon.

The detector acceptance for W and Z events is determined from a full detector simulation based on GEANT, with ISAJET as the parton-level event generator. Backgrounds arise from muons associated with jets, cosmic rays and random proportional drift tube hits, and $W \to \tau\nu, Z \to l^+l^-$ and $Z \to \tau^+\tau^-$ sources. The jet background is determined by analysing the distribution of isolation energy. Cosmic ray and combinatorial backgrounds are estimated from the drift time distribution. Punchthrough and decays in flight are negligible. The $W \to \tau\nu, Z \to l^+l^-$ and $Z \to \tau^+\tau^-$ backgrounds are estimated from Monte Carlo. Table V shows the results and the SM predictions.

3. Extraction of $B(W \to l\nu)$ and Γ(W)

Table VII shows the values of the production cross section ratio, the Z total width and leptonic width from LEP used to extract the W leptonic branching ratio. CDF extracts $B(W \to e\nu) = 0.1094 \pm 0.0033(\text{stat}) \pm 0.0031(\text{syst})$ and $\Gamma(W) = 2.064 \pm 0.0060$ (stat)± 0.059(syst). Using the SM prediction for $B(W \to l\nu)$ as a function of the top quark mass m_t, CDF extracts a 95% C.L. limit $m_t > 62$ GeV. This limit is independent of top quark decay modes and only assumes the W coupling to $t\bar{b}$.

DO extracts from the Run 1B data $B(W \to e\nu) = 0.1044 \pm 0.0015(\text{stat}) \pm 0.0020(\text{syst}) \pm 0.0017(\text{other}) \pm 0.0010(\text{NLO})$ and $\Gamma(W) = 2.169 \pm 0.031(\text{stat}) \pm 0.042(\text{syst}) \pm 0.041(\text{other}) \pm 0.022(\text{NLO})$ GeV, where the third source of uncertainty comes from uncertainties in the LEP input and the theoretical cross section ratio. The fourth source of uncertainty is due to NLO electroweak radiative corrections. DO has also combined their results from Run 1A and Run 1B. The electron channel measurements are mostly uncorrelated. Only the acceptance, the Drell-Yan correction and the NLO electroweak correction uncertainties are correlated. The measurements in the electron and muon channels are uncorrelated. The combined DO result is $R = 10.51 \pm 0.25$ and $\Gamma(W) = 2.152 \pm 0.066$ GeV. Comparing to the SM prediction $\Gamma(W) = 2.094 \pm 0.006$ GeV, DO extracts the 95% C.L. upper limit of 191 MeV on the W partial width to non-standard-model final states.

4. τ measurement

$W \to \tau\nu$ decays are identified using the hadronic decays of the τ, which result in a narrow, isolated, low-multiplicity jet, and $\not{E}_T$. CDF has used charged particle tracking to identify the τ decay, while DO has used the fine granularity of the calorimeter. Based on 1202 candidate events and an estimated total background of 222 ± 17 events, DO measures $g_\tau/g_e = 0.980 \pm 0.020$ (stat) ± 0.024 (syst), consistent with $\tau - e$ universality. Phase space effects and nonuniversal radiative corrections are negligible. Figure 19 shows a summary of recent results.

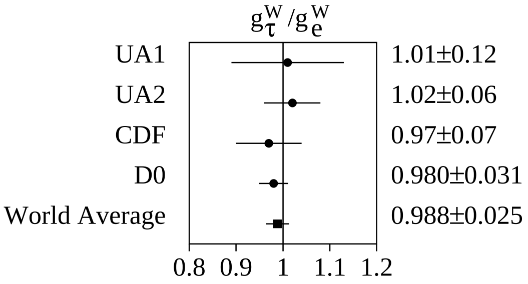

FIG. 19. Results on $\tau - e$ universality at $Q^2 = M_W^2$.

D. Lepton Charge Asymmetry

The W asymmetry is measured by CDF (Abe *et al.*, 1992, 1995b, 1998c) by counting the number of positively and negatively charged leptons as a function of lepton rapidity and constructing the asymmetry as

$$A(y_\ell) = \frac{d\sigma^+/dy_\ell - d\sigma^-/dy_\ell}{d\sigma^+/dy_\ell + d\sigma^-/dy_\ell}, \tag{25}$$

where $d\sigma$ is the cross section for W decays as a function of lepton rapidity. Since the difference in efficiencies between the ℓ^- and ℓ^+ is typically very small, its contribution to the systematic uncertainty in the ratio is also very small. In addition, CP invariance implies that the asymmetry is an antisymmetric function of rapidity, thereby allowing the positive and negative rapidity regions to be combined, further reducing systematic uncertainties due to efficiencies.

Events are collected using the typical criteria for W decays to leptons. The lepton rapidity range in accepted events extends to $|y_\ell| < 2.5$, with muons contributing in the regions $|y_\mu| < 1.1$ and $1.9 < |y_\mu| < 2.5$, and electrons contributing in the region $|y_e| < 2.4$. The high rapidity muon region, which uses the forward muon toroid detectors, is a departure from more typical CDF W analyses. Likewise, the electron contribution also makes use of higher rapidity regions than usual (the end plug calorimeter) due to the development of an alternative method of charge determination. The silicon vertex detector (SVX) is used to complement the tracking chamber for tracks with $|y| >\sim 1$. In this region, the tracking chamber efficiency and resolution degrade with increasing rapidity up to 1.8 which is the extent of the tracking chamber coverage. Beyond this, the SVX measurement of the electron trajectory, combined with the position of the EM shower in the calorimeter, provides the charge determination.

The key pieces of information in this measurement are the charge and rapidity of the lepton. Thus most of the systematic uncertainties concentrate on how well the charge is determined. Trigger efficiency dependences on E_T or charge are investigated and found to be negligible with the exception of electron triggers in the end plug calorimeter region which have an E_T dependence. A correction for this dependence is applied to the asymmetry where it varies with rapidity but is always less than 0.005 (compared to the average statistical uncertainty of 0.015). The event selection criteria are also checked for charge-dependent biases using clean W and Z events; none are found. The charge misidentification rate for low-rapidity muons is determined to be negligible; for high-rapidity muons the rate is found to be less than 1%. The charge misidentification rate for low rapidity (central) electrons is measured using Z events where both electrons have the same charge. Errors in the charge determination of central electrons are caused by overlap with electron pairs produced from a bremsstrahlung photon radiated from the W decay electron. These three electrons are colinear which confuses the pattern recognition in the tracking chamber. The wrong charge rate for high rapidity electrons is determined by looking at the tails of the SVX-determined charge measurement. These misidentification rates range from 0.2% in the central region to 10% in the highest rapidity bin. Since the charge asymmetry is diluted by picking the wrong sign, it is corrected for these rates as a function of rapidity.

The backgrounds in this analysis are the same as for most other W analyses; however, here the interest is in the charge symmetry of the background. Table VIII lists the various backgrounds by decay mode and detector region. In forward electron events, misidentified dijet events compose the largest background. This background is charge-symmetric which dilutes the asymmetry. Central electron events suffer mostly from $W \to \tau\nu \to e\nu\overline{\nu}\nu$, which is not a charge-symmetric background since it originated from a W decay. The dominant background for central muons is unreconstructed Z events where one muon is at large rapidity and escapes the tracking chamber. The backgrounds in high-rapidity muon events are larger and are split between unreconstructed Z events, misidentified dijets, and low momentum muons which are measured as high momentum muons due to the presence of noise hits. The W asymmetry is corrected for all these backgrounds as a function of rapidity.

Figure 20 shows the folded asymmetry distribution overlayed with predictions of the asymmetry using a variety of PDFs. The PDF curves are generated using the DYRAD (Giele, Glover, and Kosower, 1993) NLO QCD generator. The MRS-R2 (Martin *et al.*, 1996) and CTEQ-3M (Lai, 1995) PDF fits include roughly 20% of the full W asymmetry data set. Notice that while these fit well at low values of rapidity, they have large discrepancies at high rapidities. Re-analysis (Yang, Bodek and Fan, 1998) of NMC data (Arneodo *et al.*, 1997) leads to a modification of the $\frac{d}{u}$ ratio and a new fit, the MRS-R2 modified curve, which agrees much better overall. Recent global PDF fits (including all these data) resulted in the MRST (Martin *et al.*, 1998) set of PDFs which also agrees quite well.

At large rapidity, the W asymmetry is influenced by the p_T^W spectrum. Since DYRAD does not accurately reproduce the p_T^W spectrum at low p_T, another Monte Carlo is used to cross check the DYRAD calculation. The RESBOS generator (Balazs and Yuan, 1997) includes soft gluon resummation at all orders of perturbation theory, and since soft gluons are mainly responsible for the low end of the p_T^W distribution, it should be a good test of the DYRAD results. Using the CTEQ3M PDFs, the two generators agree in the low-rapidity region, but are slightly different in the high-rapidity region where one expects differences (see Fig. 20).

These results demonstrate that the W asymmetry is a sensitive and unique probe of the $\frac{d}{u}$ ratio and contributes significantly to parton distribution fits.

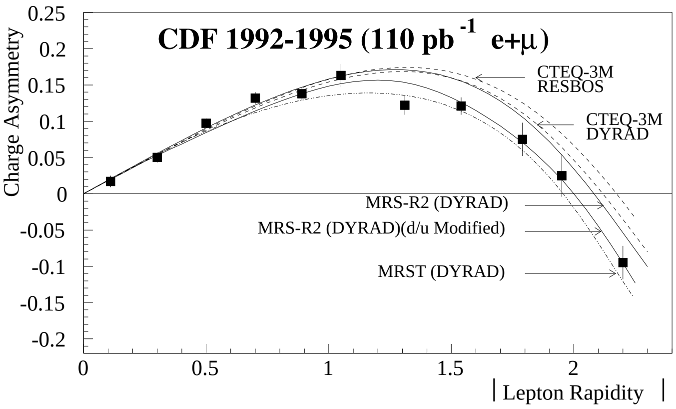

FIG. 20. The lepton charge asymmetry versus lepton rapidity. The negative rapidity region has been combined with the positive region. See the text for an explanation of the curves.

E. Transverse Momentum and Jets

QCD studies with W and Z production properties have typically been performed in two ways: (i) measuring the kinematics of the W and Z inclusively, without measuring the details of the hadronic recoil, and (ii) characterizing the hadronic recoil in terms of the identified jets and associating these jets with hard partons. We discuss measurements made by CDF and DO using both approaches.

1. W and Z boson transverse momentum

DO has measured the shape of the p_T^W distribution from the Run 1A data using the $W \to e\nu$ channel. Electrons were accepted in the central calorimeter only, $|\eta| < 1.1$, to keep the background contamination from multijet events at a reasonable level at high values of p_T^W. The electron and event selection criteria were similar to those discussed earlier in other measurements.

The trigger and selection efficiencies were determined using $Z \to e^+e^-$ data. No dependence of these efficiencies on p_T^W was found within an accuracy of 5%. A parametric Monte Carlo detector simulation, similar to the one used for the W mass and cross section measurements, is used to compare the theoretical predictions to the data. This procedure is preferred to unsmearing the data (i.e. correcting the data for resolution effects) because of the rapid variation in the dN/dp_T^W distribution near the origin. Since the resolution on the hadronic recoil (~ 5 GeV) is of the same order of magnitude as the location of the jacobian peak in dN/dp_T^W (at ~ 4 GeV, see Fig. 21), the unsmearing correction is very sensitive to the prior assumption of the true p_T^W distribution at low p_T^W. Hence smearing corrections are not applied to the data, rather the detector effects are folded into the predictions before comparing to the data.

The largest source of background in the $W \to e\nu$ candidates are QCD multijet events. As p_T^W increases, the distinctive W event signature is spoiled and the multijet background increases. The background is measured in the same p_T^W bins used for the differential cross section. The amount of multijet background in the p_T^W bins of 0-30 GeV, 30-60 GeV and >60 GeV was estimated to be $(2.9 \pm 1.6)\%$, $(20.9 \pm 11.7)\%$ and $(38.3 \pm 21.5)\%$ respectively. Additional backgrounds from top quark decays and $Z \to e^+e^-$ events were less than 5%. As a cross-check, the m_T and $\not{E}_T$ distributions in these bins were compared to the sum of signal prediction from the Monte Carlo and expected background; good agreement was found. The background subtracted data are compared to the theoretical prediction with detector simulation in Fig. 21. The agreement is good over the entire p_T range.

The p_T^W distribution provides a high statistics measurement at high p_T. At low p_T the measurement is limited by the resolution on the hadronic recoil. The measurement of p_T^Z using the decay charged leptons is complementary because it provides a more precise measurement at low p_T. In this region the QCD resummation formulation is more relevant, and at very low p_T there are non-purturbative contributions which are important to understand for the W mass measurement.

CDF and DO have both measured the p_T^Z distribution using the $Z \to e^+e^-$ events. One electron is required to be central while the second electron can be central or forward. The p_T^Z dependence of the electron identification efficiency is more important in this case than the p_T^W measurement because there are two electrons. As p_T increases, the hadronic recoil is more likely to spoil the isolation of at least one electron, thus causing loss of Z-finding efficiency. At high values of p_T^Z both electrons are boosted away from the recoil, and the Z-finding efficiency recovers. At $p_T \sim 40$ GeV, the relative loss peaks at about 8%. The background fraction in each p_T^Z bin is determined from a fit to the Z peak and sidebands with a combination of signal and background shapes.

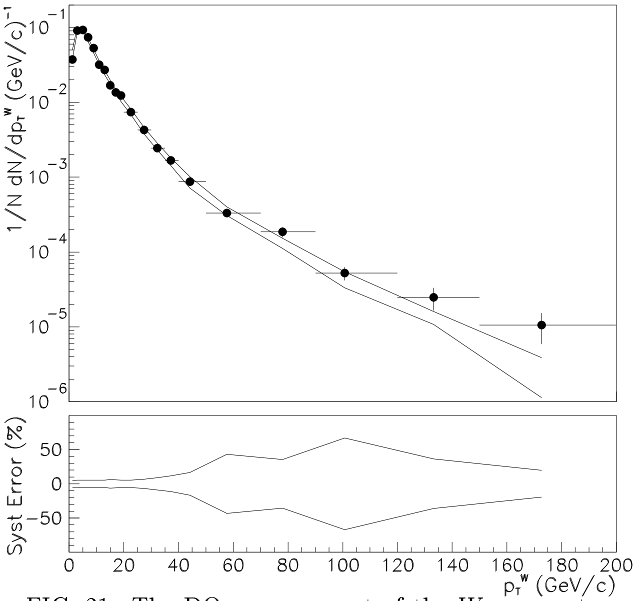

FIG. 21. The DO measurement of the W p_T spectrum (•). The error bars show the statistical uncertainty. The two lines show the theoretical calculation by Arnold and Kauffman, smeared for detector resolution, with $\pm 1\sigma$ variation of the detector modelling parameters. The fractional systematic uncertainty on the data is shown as the band in the lower plot.

The resolution corrections are important at low p_T^Z, and are well understood. DO reports the resolution correction in the $0 < p_T^Z < 1$ GeV range to be 18.5%, and decreases to $< 5\%$ above 5 GeV. CDF reports the uncertainty on the correction to be 3.6% at $p_T^Z = 0$ GeV, decreasing to 0.6% for $p_T^Z > 20$ GeV.

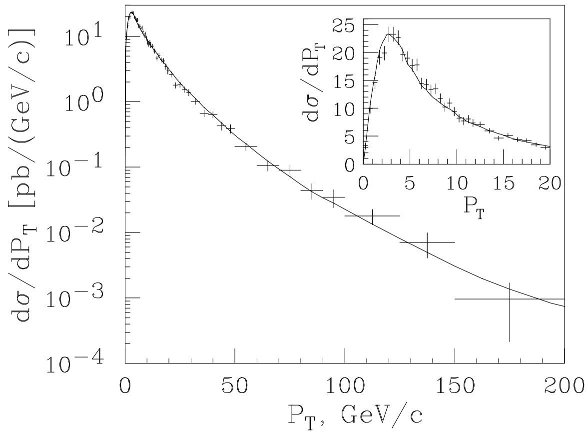

FIG. 22. The CDF measurement of the p_T spectrum of e^+e^- pairs in the mass range 66-116 GeV (Abe *et al.*, 2000a). The inset shows the $p_T < 20$ GeV region on a linear scale. The crosses are the data with all errors included except the 3.9% luminosity error. The curve is the Z-only RESBOS prediction with the cross section normalized to 248 pb.

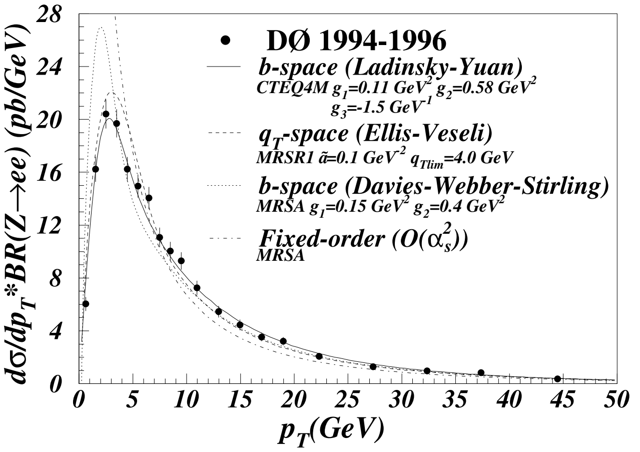

FIG. 23. The DO measurement (Abbott, *et al.*, 2000d) of the Z p_T spectrum (•), compared with theoretical calculations using resummation techniques and nonperturbative parametrizations as well as a fixed-order calculation.

Figures 22 and 23 show the fully corrected p_T^Z distribution from CDF and DO. CDF has compared their measurement to the EV (Ellis and Veseli, 1998) and RESBOS calculations, which combine the perturbative QCD calculation at high p_T with QCD resummed calculations and non-perturbative form factors at low and very low p_T. DO has done similar comparisons and also comparisons to purely perturbative $\mathcal{O}(\alpha_s^2)$ calculations. The comparisons confirm the need for the QCD resummation formulation and the non-perturbative form factor at low p_T. DO has fit their measurement to extract the g_1, g_2 and

g_3 parameters of the Ladinsky-Yuan parametrization (see Eqn. 20) of the non-perturbative form factor. The fitted values are consistent with the values extracted from fits to low energy Drell-Yan data, and the g_2 fitted value is considerably more precise than previous determinations.

2. Properties of W and Z boson + jet events

CDF and DO have measured the properties of jets accompanying W and Z bosons (Abe *et al.*, 1994, 1997b; Abbott *et al.*, 1999c). The CDF measurement of the $W+$ jets events is made from the data collected during Run 1. The jets are reconstructed in the $W \to e\nu$ events using the cone algorithm with radius $\Delta R = 0.4$. The parton energy deposited outside the cone and the energy contaminating the cone from the underlying event are corrected for. Jets are counted with $E_T > 15$ GeV and $\mid \eta \mid < 2.4$, and events that have a jet within $\Delta R = 0.52$ of the lepton are rejected. The latter requirement ensures that the jets are well separated from the electron (the cone algorithm differentiates well when the separation exceeds 1.3 times the cone radius).

The jet multiplicities are corrected for jets produced in additional $p\overline{p}$ interactions. The main background is from QCD multijet contamination, and is measured with a sample obtained by removing the electron isolation and $\not{E}_T$ requirements, and then extrapolating from the multijet-dominated region into the W signal region in $\not{E}_T$. The multijet background ranges from $(2.9 \pm 0.9)\%$ for the ≥ 0 jet sample to $(27 \pm 11)\%$ for the ≥ 4 jet sample.

The systematic uncertainties on jet counting are determined by varying the jet energy by $\pm 5\%$, the jet η by ± 0.2, the probability for extra jets from additional $p\overline{p}$ interactions by a factor of 2 (the probability is 1% for one extra jet and reduces by a factor of 6 for each additional jet), and the correction for energy contamination in the jet cone by $\pm 50\%$ (± 0.5 GeV on average). The combined uncertainty ranges from 10% for the ≥ 1 jet sample to 30% for the ≥ 4 jet sample.

The final correction to the number of $W \to e\nu + \geq n$ jet candidates includes the overall efficiency of identifying $W \to e\nu$ decays, including the acceptance, electron-jet overlap efficiency, and efficiency of online trigger and offline identification. The overlap efficiency is calculated from the data by taking $Z \to e^+e^-$ events and replacing the $Z \to e^+e^-$ decay with a simulated $W \to e\nu$ decay, preserving the boson p_T.

The data are compared with LO perturbative QCD calculations performed with the VECBOS (Berends *et al.*, 1991) program. Initial state gluon radiation, final state parton fragmentation and hadronization are performed by interfacing VECBOS to the HERWIG Monte Carlo program, with subsequent full detector simulation. HERWIG parton showers represent partial higher-order corrections to the LO VECBOS calculation, which CDF refers to as enhanced LO (ELO). CDF compares the $W + n$ jet cross sections to the ELO predictions with variation of renormalization scale, and finds agreement for $n = 2$ to 4 (see Fig. 24). The distributions of jet E_T, dijet mass and angular separation are also reasonably well described by the calculations. The statistics of the $W \to e\nu$ data are large enough to show some limitations of the ELO predictions.

Another technique of comparing data to QCD calculations is to measure the ratio of cross sections of inclusive jet production in W events to the total W cross section. CDF and DO have made measurements of the ratio $R_{10} \equiv \sigma(W+ \geq 1 \text{ jet})/\sigma(W)$. This ratio can be compared to NLO QCD predictions as a function of the jet E_T threshold E_T^{min}. The measurements have been made in $W \to e\nu$ channel. Measuring the ratio takes advantage of the cancellation of the integrated luminosity uncertainty, and the reduction of other systematic uncertainties.

The CDF measurements are made from the Run 1 data using the same criteria and algorithms as used for the $W + n$ jet cross section measurements. Results are reported for the jet E_T^{min} varied between 15 GeV and 95 GeV. The acceptance, efficiency and backgrounds are estimated for each value of E_T^{min}. The acceptance, calculated using the VECBOS generator and the CDF detector simulation, increases with E_T^{min} from 24% to 36% for $W+ \geq 1$ jet events. The acceptance for inclusive W events is $(23.9 \pm 0.5)\%$.

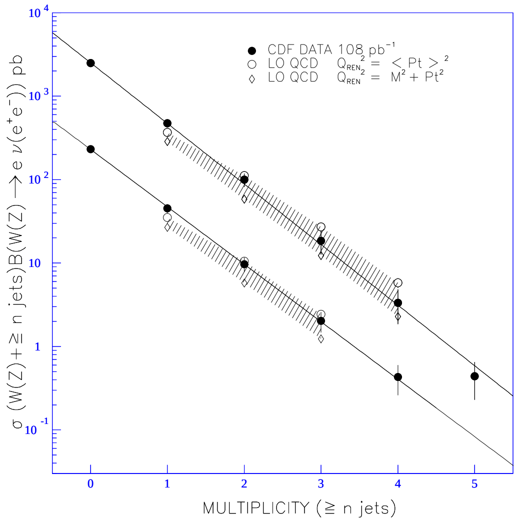

FIG. 24. The CDF measurement of cross sections for $W + n$ jets (top) and $Z + n$ jets (bottom) versus inclusive jet multiplicity. The lines are exponential fits to the data. The theory is shown as a shaded band which represents the uncertainty due to the renormalization scale. The 0 jet prediction is the Born-level calculation for inclusive W production.

The main source of background is QCD multijet production, which increases with E_T^{min} from 13% to 28%. Other backgrounds include $W \to \tau\nu \to e\nu\overline{\nu}\nu$, $Z \to e^+e^-$, $Z \to \tau^+\tau^-$, top decays, $W\gamma$ and jets from additional $p\overline{p}$ interactions. The total background increases with E_T^{min} from $(22 \pm 5)\%$ to $(44 \pm 13)\%$.

The jet energy scale uncertainty is one of the large systematic uncertainties on R_{10}, increasing from 5% to 11% as a function of E_T^{min}. The overall systematic systematic uncertainty increases from 8% to 19%.

The measured values of R_{10} are compared to perturbative NLO QCD predictions generated using the DYRAD Monte Carlo program, which calculates inclusive W production at order α_s and $W+ \geq 1$ jet at order α_s^2. The renormalization and factorization scales are set equal to the W mass. Partons with $\Delta R < 0.52$ are merged vectorially to form jets which are then smeared in E_T, η and ϕ to model detector resolution effects. Monte Carlo events with at least one jet with $E_T > E_T^{min}$ and $|\eta| < 2.4$ are used to compute R_{10} for the theory.

Figure 25 shows the measured and predicted values of R_{10} as a function of E_T^{min}. Data and theory agree well for $E_T^{min} > 25$ GeV. At low E_T^{min}, the matrix element calculation diverges and does not include soft gluon effects.

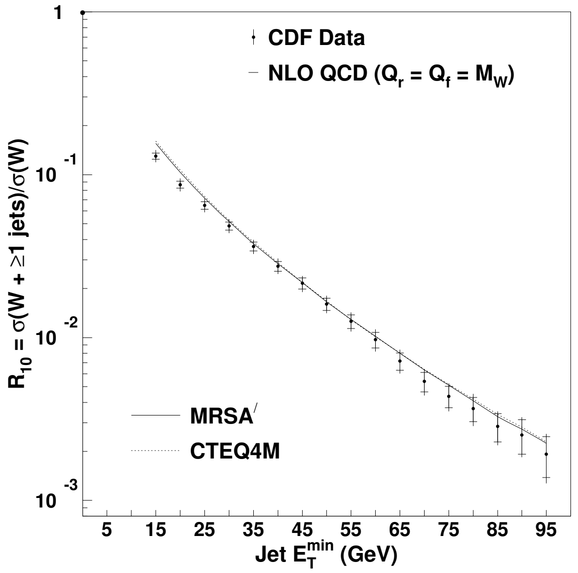

FIG. 25. The CDF measurement of R_{10} vs jet E_T^{min}, compared to the NLO QCD predictions calculated using the MRSA′ and CTEQ4M pdf's. The inner error bars include statistical uncertainties only; the outer error bars include both statistical and systematic uncertainties. The R_{10} measurements at each value of E_T^{min} are statistically correlated because the corresponding event samples are not independent.

Since the data are not corrected for out-of-cone showering, the measured R_{10} depends on the cone size. The NLO calculation approximates the jet shape by producing up to two final-state partons. The agreement between data and theory depends on how well the jet shape is reproduced by the theory. The effect of changing the parton clustering algorithm is found to be small. The NLO predictions are found to be much less sensitive to changes in the factorization and renormalization scales than LO predictions: a factor of two variation in the scales changes R_{10} by 5% at NLO and 15% at LO.

The data are compared to theory predictions for various input values of $\alpha_s(M_Z)$. There is agreement for $\alpha_s(M_Z)$ values between 0.105 and 0.130. The sensitivity of the predicted R_{10} to α_s is not large enough to permit an extraction of α_s from the current measurements. DO performed the same measurement with the Run 1A data, with a jet cone radius of 0.7 and $E_T^{min} = 25$ GeV. The DO measurement of R_{10} is one standard deviation higher than the prediction (Abachi *et al.*, 1995d).

F. Heavy and Right-handed W Bosons

Heavy right-handed gauge bosons have been searched for in the $l\nu$ and $eejj$ channels. In the former channel, one assumes that right-handed neutrino from the $W_R \to l_R\nu_R$ process be light ($M_{\nu_R} \ll M_{W_R}$) thus making its decay products highly boosted and not easy to separate. These searches do not distinguish between left-handed and right-handed W decay topologies and are referred to as heavy W' boson searches. Previous direct searches for $W' \to l\nu$ decays in $p\overline{p}$ experiments (Ansari *et al.*, 1987a and Albajar *et al.*, 1989) had set a lower limit for the mass of the W' of 220 GeV at 90% C.L. An earlier CDF search using Run 0 data (Abe *et al.*, 1991c) measured $M_{W'} > 520$ GeV at 95% C.L.

In the latter channel, one makes definite assumptions in the subsequent decay of the ν_R, depending on the mixing between the right and left-handed gauge bosons. For minimal mixing, the ν_R decays into an electron and an off-shell W_R^*, which in turn has only the $q\overline{q}'$ channel open assuming that the electron ν_R is the lightest among the right-handed neutrinos. For large mixing, the ν_R preferably decays into an electron and a left-handed W which goes into $q\overline{q}'$ in 2/3 of the cases. In both scenarios, the most abundant final state involves two electrons and two jets coming from the quarks. The only previous W_R direct search at hadron colliders was performed by the UA2 Collaboration (Alitti *et al.*, 1993) and resulted in a lower limit $M_{W_R} > 261$ GeV for any value of the ν_R mass.

1. Search for heavy W' bosons

Both CDF (Abe *et al.*, 1995d) and DO (Abachi *et al.*, 1995a) have pursued helicity-independent searches for direct production of W' in the electron channel using Run 1A data. They assume that the W' has standard couplings to fermions, that the $W'WZ$ coupling is suppressed, and that the right-handed neutrinos are light noninteracting and stable. DO allowed events coming from $W' \to \tau\nu \to e\nu\nu$ in the signal definition. CDF has also searched for W' production in the muon channel using the full Run 1 sample (Abe *et al.*, 1999c). In all of these analyses the m_T distribution is searched for evidence of a jacobian peak above the W mass peak. The limits on the production and decay rates of such a massive object are usually calculated relative to the production and decay rate of the SM W boson, thus avoiding many of the uncertainties associated with an absolute measurement.

Table IX shows the number of $l\nu$ events selected by the above searches with requirements analogous to the W mass analysis. Background sources other than SM leptonic W decays come from $W \to \tau\nu$, $Z/\gamma \to ll$, $Z/\gamma \to \tau\tau$ and QCD di-jets events in which one jet fakes an electron or a muon and the second is poorly measured, giving rise to substantial $\not\!\!E_T$. The shape of the first three sources is extracted from MC simulations while their size is determined using measured production rates and branching fractions to these final states. The QCD background contribution is estimated directly from the data. Figure 26 shows the transverse mass distribution for the CDF $W' \to \mu\nu$ selected sample. Superimposed is the unbinned maximum likelihood fit to the m_T distribution between 40 and 2000 GeV assuming only contributions from left-handed $W \to \mu\nu$ decays and from the other known background sources. There is good agreement over the whole spectrum and no excess is observed in the high m_T region to indicate the presence of $W' \to \mu\nu$ decays. The same qualitative agreement is found for the $W' \to e\nu$ searches as shown by the number of observed versus expected events in the high m_T region presented in Table IX.

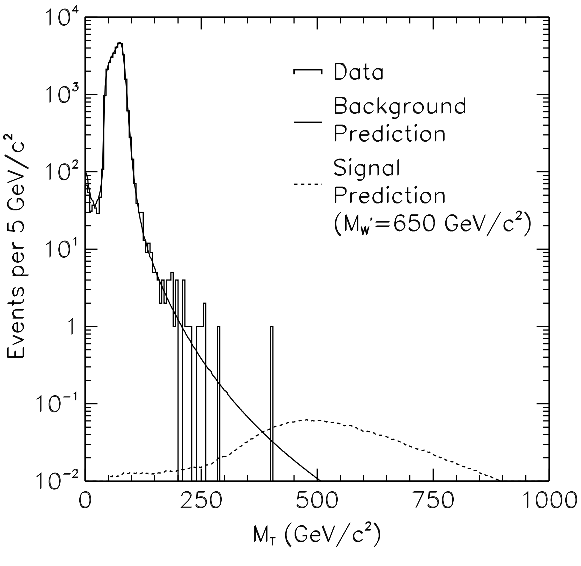

FIG. 26. Transverse mass spectrum in the CDF $W' \to \mu\nu$ search. The background fit (full line) is superimposed on the data (histogram). The signal (dashed line) expected for a W' with a mass of 650 GeV is also shown.

The $q\overline{q} \to W'$ production diagram is simulated using LO or NLO generators with MRS-D$'$ (Martin *et al.*, 1993) or CTEQ 4A1 (Lai *et al.*, 1997) PDFs for the electron and muon decay channels, respectively. Whenever a LO generator is used, higher order diagrams for W' production are taken into account by modelling the p_T of the W' at production according to the measured W spectrum. To extract a limit on the mass of the heavy boson, the kinematic and geometric acceptance for the signal is estimated as a function of $M_{W'}$ after passing the generated W' events through the detector simulation.

The limit on the relative contribution of a W' is obtained by fitting the data distribution to the sum of the background, including $W \to l\nu$, and the m_T distribution expected for a W' of a given mass. The resulting likelihood function is used to set a 95% CL upper limit on the ratio of W' candidates to the SM contribution. The limits are insensitive to the assumed width of the W' since the width is dominated by the detector resolution. Systematics uncertainties in the acceptance, backgrounds and m_T shape distributions coming from different PDF choices are incorporated into the probability density functions as Gaussian distributed errors. The 95% CL limits shown in Table IX are obtained by plotting the $\sigma(p\overline{p} \to W') \cdot B(W' \to l\nu)$ limit as a function of $M_{W'}$ and finding the point where it intercepts the theoretical curve assuming standard couplings to fermions.

2. Search for right-handed W bosons

DO performed a direct $eejj$ search for W_R bosons with mass greater than 200 GeV which decay into an electron and a heavy right-handed neutrino ν_R using Run 1 data (Abachi *et al.*, 1996a).

Two different analyses are performed depending on the ratio $R = M_{\nu_R}/M_{W_R}$. If $R \leq \frac{1}{2}$, the electron transverse energy E_T^e is searched for a jacobian peak indicative of the presence of the W_R (peak search). If on the other hand $R \geq \frac{1}{2}$, the decay products of the more massive and thus slower ν_R are expected to be well separated, making possible the identification of the two electrons and two jets in the event. A simply counting experiment is then performed after requiring the two electrons to give a mass outside the Z peak ($eejj$ search).

The peak search finds 101 events with $E_T^e > 100$ GeV. After modelling backgrounds from large p_T W and Z events and misidentified QCD di-jet events, a simultaneous fit to the E_T^e and m_T distributions is used to extract information on the probability that events coming from

W_R decays are in the sample. No evidence of an excess in the high E_T^e or m_T regions is found. The acceptance for the E_T^e distribution of the signal was calculated for a grid of points in the (M_{W_R}, M_{ν_R}) plane using a MC simulation. The 95% CL upper limit on the number of W_R events is converted into an upper limit for the $\sigma(p\overline{p} \to W_R) \cdot B(W_R \to e\nu_R)$ by normalizing to the measured σ_W and σ_Z and to the observed number of W and Z events found in the simultaneous fit to the E_T^e and m_T distributions. Since this search looks only at the inclusive high E_T^e distribution, it is sensitive to both the right-handed and left-handed W bosons. The point where the 95% CL upper limit $\sigma \cdot B$ curve intersects the theoretical curve for the standard coupling scenario gives a limit on any helicity W' gauge boson. For $M_\nu \ll M_{W'}$, the DO limit is $M_{W'} > 720$ GeV.

For the $eejj$ search, events with two isolated electrons with $E_T > 25$ GeV and two or more jets with $E_T > 25$ GeV are selected. Of the 22 events passing these cuts, only two survive the requirement that the invariant mass of the two electrons be outside the M_Z peak. These two W_R candidates are consistent with the estimated total background of 3.08 ± 0.78 events obtained from Monte Carlo studies of Z + jets, $t\bar{t}$ and QCD events. As for the peak search, the signal acceptance is calculated with the MC for a grid of points in the (M_{W_R}, M_{ν_R}) plane for both the the small and large mixing case. An upper limit on $\sigma \cdot B$ was obtained using a Bayesian approach (Particle Data Group, 1994) with a flat prior distribution. Figure 27 summarizes the results of the DO searches in terms of the excluded region in the (M_{W_R}, M_{ν_R}) plane.

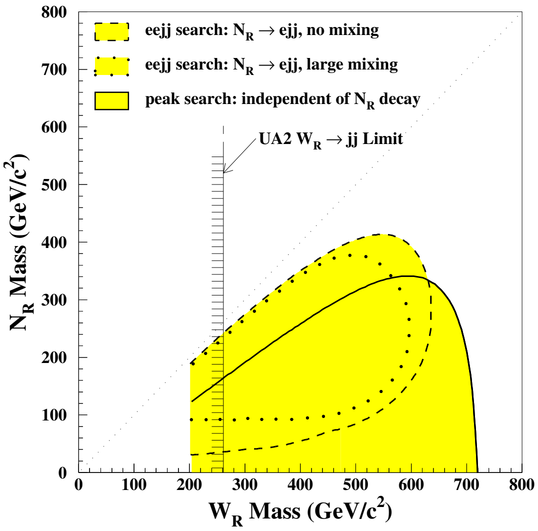

FIG. 27. Excluded regions at 95% CL of M_{W_R} vs M_{ν_R} for the DO searches assuming standard coupling to fermions. Also shown is the previous UA2 limit.

G. Rare Decays

Two rare decays, $W \to \pi\gamma$ and $W \to D_s\gamma$, have been searched for at hadron colliders. The former has a predicted decay branching fraction of $\sim 3 \times 10^{-8}$ while the latter has a predicted branching fraction of $\sim 1 \times 10^{-8}$ (Arnellos, Marciano, and Parsa, 1982). These decay rates are about 6 orders of magnitude smaller than the leptonic decay rates.

1. $W \to \pi\gamma$

The upper limit on the decay rate for $W \to \pi\gamma$ has been measured by CDF, UA2, and UA1 (Abe *et al.*, 1998a; Alitti *et al.*, 1992c; Albajar *et al.*, 1990). This section describes the most recent CDF measurement from Run 1B.

A $W \to \pi\gamma$ event is characterized by a high E_T photon and a high p_T pion. The pion appears as a high E_T jet with a single high p_T track pointing to the jet. Background events are predominantly QCD direct photon events (a photon back-to-back with a quark/gluon) where the jet fragmentation process produces a single charged pion.

The trigger selects events with photon candidates with $E_T > 23$ GeV. Since this energy threshold is relatively high, the energy dependence of the trigger efficiency is combined with the expected energy spectrum of photons originating from the $W \to \pi\gamma$ process to obtain an overall trigger efficiency.

The offline analysis consists of two paths: one which selects photons, and one which selects pion candidates. A photon is defined as an electromagnetic shower without an associated track in the tracking chamber. Further requirements are placed on the shape of the shower, requiring consistency with shower shapes measured in test-beam data. The shower should be isolated from neighboring energy deposits by requiring less than 4 GeV in a cone of $\Delta R = 0.7$ around the photon. The photon direction is reconstructed from the position of the shower and the location of the event vertex.

The pion search looks for jets with a single high p_T track pointing in the direction of the jet. Both the jet and the associated track are required to have $E_T > 15$ GeV. In this case, the track is required to be isolated with no other tracks having $p_T > 1$ GeV/c in a cone of $\Delta R = 0.7$ around the pion candidate track. Since a pion deposits most of its energy through hadronic interactions, the hadronic calorimeter is required to contribute more than 20% to the total energy of the jet. To further correlate the track with the jet, the charge fraction, which is the ratio of track p_T to jet E_T, must be greater than 1.0.

After combining the photon and pion searches, several additional requirements are made. The pion track and the photon must be separated in ϕ by more than 1.5 radians to remove accidental overlaps between say a jet and an electron from a W leptonic decay. A candidate sample of 28 events remains after adding a final requirement that there be no other jets with $E_T > 15$ GeV. Three of these 28 events are within the W pole region defined as 3 times the mass resolution (± 8.7 GeV).

Leptonic $W \to e\nu$ decay events are used to determine selection efficiencies. $W \to e\nu$ events are selected from the single track jet data comprising the first element of the pion search. An additional requirement that the jet contains at least 15 GeV of electromagnetic energy almost exclusively selects $W \to e\nu$ events. The neutrino momentum in these events is computed from the electron momentum, $\not\!\!E_T$ and the W mass. There are in general two solutions, either of which may be unphysical and not used. If both are valid, the choice is made by fiducial requirement of $|\eta(\nu)| < 1.1$, or random selection if both satisfy the fiducial cut.

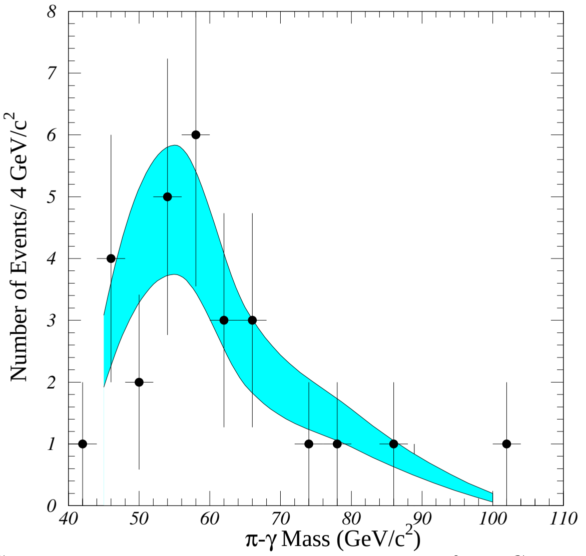

FIG. 28. The $\pi\gamma$ invariant mass distribution from CDF. The shaded region is the expected distribution from backgrounds.

Using the $W \to e\nu$ events, the photon shower shape efficiencies are determined from the electron shower shapes and compared to Monte Carlo simulations. A systematic uncertainty is assigned to account for data - Monte Carlo differences and to allow for electron brehmsstrahlung. The photon isolation cut efficiency is measured using an isolation cut around the neutrino direction, with a systematic uncertainty reflecting the differences between isolation around the neutrino and around the electron. An embedded simulated pion with the same momentum as the neutrino is used to determine the jet EM fraction and charged fraction pion selection efficiencies. Again differences between data and Monte Carlo contribute systematic uncertainties. Here, as in the photon case, the isolation efficiency is determined by looking at the isolation around the neutrino. The overall efficiency times acceptance is taken from Monte Carlo and scaled by the difference between it and the data. It amounts to 0.038 ± 0.005 with the bulk of the losses coming from geometric acceptance.

The dominant direct photon background is estimated from the data by relaxing the single track cut, and instead requiring at least 3 tracks whose net charge is ± 1. Since there is more than one track now, the multiple tracks (those with $p_T > 1$ GeV) have their momenta summed and this momentum is used in the charged fraction criteria. It has been found that the number of events observed is a linear function of the number of tracks in the momentum sum. Thus, extrapolating to 1 track determines the number of background events. This extrapolation is carried out for both the 3σ mass region around the W and elsewhere (from 40 to 110 GeV). The extrapolated numbers are scaled such that the number of background events in the regions excluding the W agree with the 25 observed events. The number of background events expected in the W signal region is 5.2 ± 1.5 to be compared with 3 observed events (see Fig. 28).

From these numbers a limit of $\sigma \cdot B(W \to \pi\gamma) \leq 1.7$ pb is obtained at a 95% confidence level, or alternatively $\Gamma(W \to \pi\gamma)/\Gamma(W \to e\nu) \leq 7 \times 10^{-4}$.

2. $W \to D_s\gamma$

The decay rate for $W \to D_s\gamma$ is expected to be about a factor of 3 larger than the decay rate for $W \to \pi\gamma$, but because the D_s has a large number of decay modes, and only a small number are open to experimental identification, the actual sensitivity is much smaller than the $W \to \pi\gamma$ case. There is only one measurement currently of this decay mode, published by CDF (Abe *et al.*, 1998b) using Run 1B data.

Like the $W \to \pi\gamma$ rare decay, the $W \to D_s\gamma$ decay also contains a high E_T photon, but instead of containing a single-track jet produced by the pion, it contains a collection of final states resulting from the decay of the D_s. Two decay modes of the D_s are utilized in this measurement: $D_s^\pm \to \phi\pi^\pm \to K^+K^-\pi^\pm$ and $D_s^\pm \to \overline{K^{*0}}K^\pm \to K^-\pi^+K^\pm$. These constitute about 4% of the D_s width.

The data collection follows the same path as $W \to \pi\gamma$ decays, including trigger efficiency calculations. The photon selection criteria and their efficiencies are also shared with the $W \to \pi\gamma$ analysis. It is only the fact that the D_s decays quickly and the pion doesn't which differentiates the two analyses.

The identification of the D_s involves simple combinatoric mass fits, first reconstructing either the ϕ or $\overline{K^{*0}}$ and then the D_s using tracks with $p_T > 1$ GeV. The p_T of the reconstructed intermediate state is required to be greater than 10 GeV, and the p_T of the D_s is required to be greater than 22 GeV (consistent with the photon). There are also D_s sideband fits which are used for background determinations. A further requirement is that the D_s be isolated in much the same way as the pion was: there should be no other tracks with $p_T > 1$ GeV in a cone of $\Delta R = 0.7$ around the D_s. There are 4 D_s events left in the W pole region (3σ in this analysis is ± 7.9 GeV) and 4 D_s sideband events. The D_s signal events contain 1 ϕ channel and 3 $\overline{K^{*0}}$ channel events.

The D_s fitting efficiency is determined from a Monte Carlo simulation using a combination of PYTHIA and the CLEO Monte Carlo together with a full detector simulation. Track-finding efficiencies are determined by embedding simulated tracks in data and convoluting the measured efficiencies with the p_T spectrum from the Monte Carlo. As with the $W \to \pi\gamma$ analysis, the track isolation efficiency is measured using the neutrino direction in the $W \to e\nu$ sample.

The net efficiency times acceptance is 0.069 ± 0.005 of which the dominant loss is again due to acceptance. Combining this with the 4(4) signal(background) events, results in a limit of $\sigma \cdot B(W \to D_s\gamma) \leq 27.4$ pb at 95% C.L., or alternatively $\Gamma(W \to D_s\gamma)/\Gamma(W \to e\nu) \leq 1.1 \times 10^{-2}$. Figure 29 shows the signal and sideband mass distributions together with the $W \to D_s\gamma$ simulation normalized to 4 signal events.

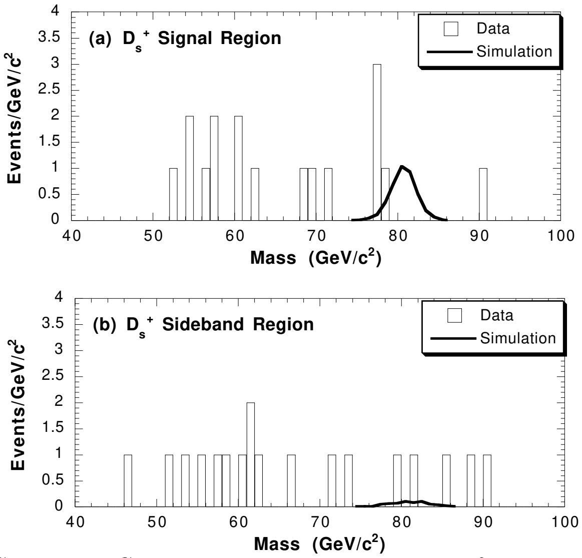

FIG. 29. The CDF invariant mass distributions for signal and sideband regions. The curve is the $W \to D_s\gamma$ Monte Carlo simulation normalized to 4 signal events.

H. Trilinear Gauge Couplings

Trilinear W boson couplings are a direct consequence of the gauge invariance of the standard model due to the non-abelian character of the $SU(2)_L$ isospin symmetry group. These couplings can be studied directly at the Tevatron in events with $W\gamma$, WW and WZ diboson production. The presence of anomalous couplings manifests itself in an increase of the total diboson cross section especially at large values of the diboson invariant mass. This can be understood because the trilinear couplings contribute via the s-channel diagram whose effect is particularly strong in the central part of the detectors. Experimental limits on anomalous couplings are obtained by comparing the measured cross section or the shape of event kinematical distributions to the SM and to the effective lagrangian predictions for anomalous couplings. In the following we will discuss the distributions which are expected to be more sensitive to the anomalous coupling parameters g_1^V, λ_V and $\Delta\kappa_V$.

The NLO cross-sections for diboson production in $p\overline{p}$ colliders have been calculated for the $W\gamma X$ (Ohnemus, 1993 and Baur, Han, and Ohnemus, 1993), the WWX (Ohnemus, 1991a and Baur, Han, and Ohnemus, 1996), and the WZX final state (Ohnemus, 1991b, and Baur, Han, and Ohnemus, 1995). The SM predictions for $\sigma(WW)$ and $\sigma(WZ)$ are 9.5 pb and 2.5 pb, respectively. For the $W\gamma$ final state, the predictions are usually for the cross section times the branching fraction $B(W \to l\nu)$, integrated over the photon E_T spectrum above a minimum $E_T^{min}(\gamma)$. It should be remarked that at the Tevatron energies, the $\mathcal{O}(\alpha_s)$ corrections are responsible for an $\approx 30\%$ increase with respect to the LO cross section. The NLO effects leave the shape of the event kinematic variables generally unchanged. Therefore, when studying these final states, it is customary to multiply distributions obtained from LO Monte Carlo generator samples by a K-factor of $1 + \frac{8}{9}\pi\alpha_s(M_W^2) \approx 1.34$. This leads to conservative estimates of the limits if the order-α_s corrections are larger in the high diboson invariant mass or boson p_T regions used for the coupling measurements.

The standard model predicts that the $p\overline{p} \to W\gamma X$ process has vanishing amplitudes for $\cos\Theta = \pm 1/3$, where Θ is the angle between the scattered photon and the quark direction in the $W^{\mp}\gamma$ center-of-mass frame. This is known as the amplitude zero effect and is partially eliminated by the presence of anomalous couplings. As a consequence, the photon E_T spectrum is a very sensitive variable to any deviation from SM predictions because the average photon E_T increases considerably if anomalous couplings exist. In general $WW\gamma$ studies have higher sensitivity to the λ_γ than to the $\Delta\kappa_\gamma$ coupling.

The $p\overline{p} \to WWX$ events are selected using leptonic decays of both or at least one W boson. The former are cleaner but suppressed by the additional $B(W \to l\nu)$ factor. The latter has larger background contamination from W + 2 jet events and are practically impossible to distinguish from the WZ events. The dilepton p_T spectra and the W transverse mass distributions are most sensitive to trilinear couplings for the two classes of events.

WW production has contributions from both $WW\gamma$ and WWZ vertices. To derive limits on the anomalous trilinear contributions, it is customary to assume some relations between the $WW\gamma$ and WWZ couplings so as to reduce the number of independent parameters. Common choices are: SM values for one set of parameters, equal $WW\gamma$ and WWZ couplings, or the HISZ relations (Hagiwara *et al.*, 1993) which specify λ_Z, κ_Z and g_1^Z in terms of the independent variables λ_γ and κ_γ. In general, one expects WW production to be considerably more sensitive to $\Delta\kappa_V$ than $p\overline{p} \to W\gamma X$ and $p\overline{p} \to WZX$ processes.

The $p\overline{p} \to WZX$ process is sensitive only to the WWZ vertex but suffers from a low cross-section. It has been found that in the SM at tree level WZ production exhibits an approximate amplitude zero at $\cos\theta \approx \frac{1}{3}\tan^2\theta_W$ which makes the p_T^Z spectrum particularly sensitive to anomalous couplings.

At the Tevatron, events with a $W\gamma$, WW or WZ final state are isolated by requiring a leptonic decay of at least one of the massive bosons. Analyses have been performed in the following channels:

1. $W\gamma \to l\nu\gamma$
2. $WW \to l\nu l\nu$
3. $WW/WZ \to l\nu jj$ and $WZ \to jjl^+l^-$
4. $WZ \to l\nu l^+l^-$

where l stands for either e or μ.

1. $W\gamma \to l\nu\gamma$ analysis

The $p\overline{p} \to W\gamma X$ process has the largest cross section but also an important background contribution from radiative W decays in which the charged lepton radiates a photon. In these events the photon and the lepton tend to be collinear, hence the need to cut on their angular separation $\Delta R_{l\gamma} > 0.7$. The contribution from this background can be further reduced by a cut on the $W\gamma$ transverse mass since in radiative decays the $l\nu$ pair and the photon form a system with transverse mass $m_T(l\nu\gamma)$ below the W mass whereas for $W\gamma$ production the $m_T(l\nu\gamma)$ is larger than M_W. Possible contamination from the process $q_1 g \to W q_2$ with photon bremsstralung off the final-state quark can be efficiently suppressed by requiring the photon to be isolated (Ohnemus and Stirling, 1993).

The DO results from the full Run 1 statistics (Abachi *et al.*, 1997a) are shown in Table X. The CDF Collaboration has published the cross section measurement and limits on anomalous couplings based on Run 1A data (Abe *et al.*, 1995f). Table X shows preliminary results from Run 1B data (Benjamin, 1996).

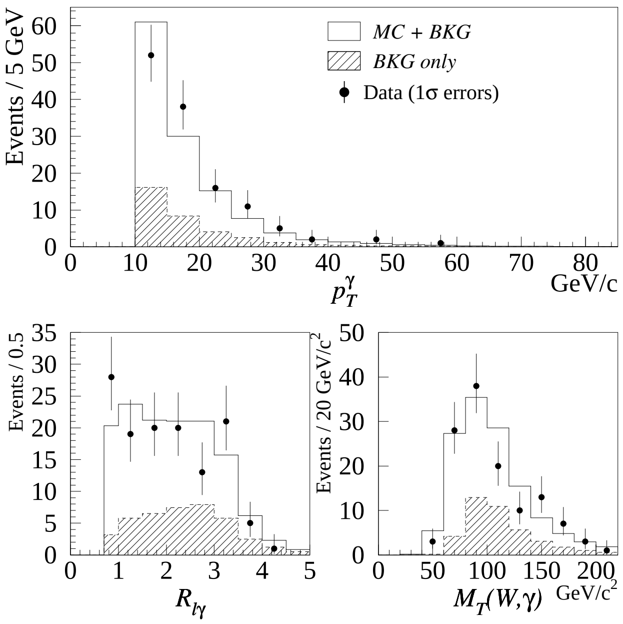

FIG. 30. Photon E_T spectrum for DO $W\gamma \to l\nu\gamma$ events (top), the lepton-photon angular separation (bottom left) and the $W\gamma$ transverse mass distribution (bottom right).

The major source of background in $W\gamma \to l\nu\gamma$ events arises from neutral mesons misidentified as photons or genuine photon production in W + jet events. Both CDF and DO estimate this contamination by measuring in an independent sample of multijet events the fraction of jets which pass the photon identification criteria. This probability $P(jet \to \gamma)$ decreases with the E_T of the photon and is of order 10^{-4} to 10^{-3} after correcting for the presence of prompt γ in the jet sample. This prompt photon contribution is removed using cuts on the longitudinal and transverse profile of the calorimeter showers. Other backgrounds like $Z\gamma \to ll\gamma$ events where one lepton is outside the detector fiducial region, or $W\gamma \to \tau\nu\gamma$ events are estimated using MC calculations.

The cross section times the branching fraction $\sigma(W\gamma) \times B(W \to l\nu)$ measured by both experiments agrees well with the SM expectation, as seen in Table X. Figure 30 shows the combined DO electron and muon $W\gamma$ sample.

Limits on the $WW\gamma$ anomalous coupling parameters are derived from a binned maximum likelihood analysis of the observed photon E_T spectrum. The best results are obtained by the DO Collaboration which sets the 95% C.L. limits for the individual coupling parameters at $-0.93 < \Delta\kappa_\gamma < 0.94$ ($\lambda_\gamma = 0$) and $-0.31 < \lambda_\gamma < 0.30$ ($\Delta\kappa_\gamma = 0$), assuming a form factor scale $\Lambda = 1.5$ TeV. These couplings have a simple physical interpretion in terms of the W magnetic dipole moment $\mu_W = \frac{e}{2M_W}(1 + \kappa_\gamma + \lambda_\gamma)$ and electric quadrupole moment $Q_W^e = -\frac{e}{M_W^2}(\kappa_\gamma - \lambda_\gamma)$. Figure 31 shows the two-dimensional 95% CL limits in the (μ_W,Q^e_W) space.

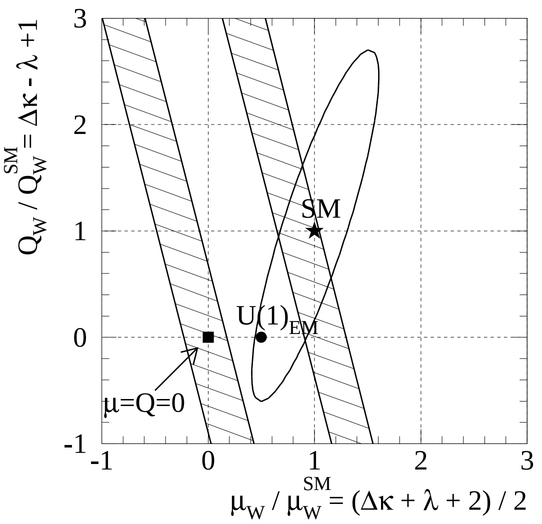

FIG. 31. DO limits in terms of the W magnetic dipole (μ_W) and electric quadrupole (Q_W) moment, normalized to their standard model values. The shaded regions are allowed from the CLEO $b \to s\gamma$ measurement. The points shows the minimal coupling value.

2. $WW \to l\nu l\nu$ analysis

The analysis starts by identifying events with two isolated e^+e^- or $\mu^+\mu^-$ or $e^\pm\mu^\mp$ leptons and a minimum $\not{E}_T$ of 25 GeV. This stiff cut on the $\not{E}_T$ reduces both the $Z \to \tau\tau$ and Drell-Yan ($\gamma/Z \to e^+e^-$, $\mu^+\mu^-$) backgrounds. Events are rejected if the invariant mass of the e^+e^- or $\mu^+\mu^-$ pair is in the range 75-105 GeV to remove any contamination from events containing a Z boson in the final state. The biggest remaining source of contamination comes from $p\overline{p} \to t\overline{t} + X$ where the W from both top quarks decay leptonically. To remove it, CDF rejects events if they contain any jet with $p_T > 10$ GeV while DO requires that the hadronic energy in the calorimeter, $\vec{E_T}^{had} = -(\vec{E_T}^{l_1} + \vec{E_T}^{l_2} + \vec{\not{E}_T})$, be less than 40 GeV.

The CDF Collaboration analyzed their full Run 1 data sample and found 5 candidates, two ee and three $e\mu$ (Abe *et al.*, 1997a). The estimated background is 1.2±0.3 events which gives a $\sigma(p\overline{p} \to WW) = 10.2^{+6.3}_{-5.1}$(stat)±1.6(syst) pb. The DO Collaboration analysis also finds 5 events (two ee, one $\mu\mu$ and two $e\mu$) in Run 1 with 3.1 ± 0.4 events expected from background sources (Abbott *et al.*, 1998b; Abachi *et al.*, 1995b). This is in agreement with the SM expectation of 1.9±0.1 events assuming a $\sigma(p\overline{p} \to WW)$ of 9.5 pb.

Limits on the WWV coupling parameters for CDF are obtained by comparing the total cross section to the Monte Carlo predictions. DO performs a binned maximum likelihood fit to the observed two-dimensional spectra of lepton p_T and obtains the following 95% CL limits, using a form factor scale $\Lambda = 1.5$ TeV: $-0.62 < \Delta\kappa < 0.77$ ($\lambda_\gamma = \lambda_Z = 0$) and $-0.52 < \lambda < 0.56$ ($\Delta\kappa_\gamma = \Delta\kappa_Z = 0$).

3. $WW/WZ \to l\nu jj$ and $WZ \to jjl^+l^-$ analysis

The measurements of anomalous three-boson couplings in events in which a W decays leptonically and the second W or Z decays hadronically are a natural complement to the analysis presented in the previous section. The $WW/WZ \to l\nu jj$ final state benefits from a larger branching fraction and from a larger detector acceptance to jets. The backgrounds on the other hand are a challenge, expecially from $W+ \geq 2$ jets decays with $W \to l\nu$ and QCD multijet events where one of the jets is misidentified as an electron or was accompanied by a muon.

The CDF Collaboration analyzed the Run 1A data (Abe *et al.*, 1995f) but also allows events in which the Z decays leptonically and the W hadronically. To keep the background under control, the analysis is restricted to the high boson p_T region where the sensitivity to anomalous coupling is maximal. The p_T^W cut is set high enough to limit the number of background events to less than one in order to make background subtraction unnecessary. The candidate W or Z hadronic decay must have the two highest E_T jets with $E_T^J > 30$ GeV and a dijet invariant mass 60 GeV$< m(JJ) <$110 GeV. The p_T of the two-jet system must be $p_T(JJ)$ >130 GeV in W leptonic decays and $p_T(JJ) > 100$ GeV in Z leptonic decays. Using SM couplings, one predicts 0.13 $WW/WZ \to l\nu jj$ events with $N_{obs} = 0$ and 0.2 $WZ \to jjll$ events with $N_{obs} = 1$, consistent with no excess of events.

The best Tevatron limits on the anomalous WWV couplings using $WW/WZ \to l\nu jj$ events are obtained by DO. The DO analysis (Abachi *et al.*, 1997b; Abbott *et al.*, 1999b) makes use of the full Run 1 data sample and differs from the CDF analysis only in that it requires the presence of at least two jets with $E_T^J > 20$ GeV for which the largest invariant mass combination should be in the range 50 GeV$< m(JJ) <$110 GeV. No cut is applied on the p_T of the two jets; instead the limits on the couplings are obtained from a binned likelihood fit to the observed $p_T(l\nu)$ spectrum with the sum of the signal and background predicted by the Monte Carlo. The total number of observed events is consistent with the SM prediction, as shown in Table XI. Assuming that the $WW\gamma$ and WWZ couplings are equal, DO obtains $-0.47 < \Delta\kappa < 0.63$ ($\lambda = 0$) and $-0.36 < \lambda < 0.39$ ($\Delta\kappa = 0$) from $WW/WZ \to e\nu jj$ events, and $-0.62 < \Delta\kappa < 0.78$ ($\lambda = 0$) and $-0.45 < \lambda < 0.46$ ($\Delta\kappa = 0$) from $WW/WZ \to \mu\nu jj$ events. These limits are calculated with a form scale factor $\Lambda = 1.5$ TeV and, while comparable for λ, are significantly better for the $\Delta\kappa$ parameter than the limits obtained from the $W\gamma \to l\nu\gamma$ analysis.

4. $WZ \to l\nu l^+l^-$ analysis

DO has performed an analysis of WZ production in the $p\overline{p} \to e\nu eeX$ and $p\overline{p} \to \mu\nu eeX$ events using a data sample corresponding to an integrated luminosity of approximately 90 pb^{-1} (Abbott *et al.*, 1999b). This very unusual signature of three isolated high p_T leptons and $\not{E}_T$ is expected to be background free, except for objects misidentified as leptons, like Z + jet events, where $Z \to ee$ and the jet mimics an electron or produces a muon. But very few events are expected given the low WZ production cross section and the high branching ratio suppression.

Data-based methods were used to estimate such backgrounds and gave the results reported in Table XII. For standard model WZ production the efficiencies have been found to be $(16.9 \pm 1.4)\%$ and $(11.5 \pm 1.4)\%$ for the $e\nu ee$ and $\mu\nu ee$ channels, respectively. A 95% C.L. upper limit of 47 pb on the WZ cross section is estimated based on the only observed event in the $e\nu ee$ final state. A log-likelihood method was used to derive limits on the couplings once the probability of observing one event was determined. The value of the form factor Λ was chosen to ensure that the anomalous coupling limit is less than the unitarity limit. This analysis was most sensitive to λ_Z and Δg_1^Z. Setting $\Lambda = 1$ TeV, the 1-dimensional 95% C.L. limits from $WZ \to l\nu ee$ events are $|\Delta g_1^Z| < 1.63$ ($\lambda_Z = 0$, $\Delta\kappa_Z = 0$) and $|\lambda_Z| < 1.42$ ($\lambda_Z = 0$, $\Delta\kappa_Z = 0$).

CDF has reported evidence of a $WZ \to e\nu ee$ candidate but no limits has been derived from this event (Nodulman, 1996).

5. DO combined WWV analysis

DO has performed a simultaneous fit to the most sensitive distributions to anomalous WWV couplings (Abbott *et al.*, 1998b, 1999b) thus obtaining the most stringent Tevatron limits on the λ and $\Delta\kappa$ parameters. The distributions used are the $p_T(\gamma)$ spectrum of the $W\gamma$ events, the $p_T(l_1)$ and $p_T(l_2)$ of the two leptons in $WW \to l\nu l\nu$ events, the $p_T(l\nu)$ of the W boson final states in $WW/WZ \to l\nu jj$ events and the observed number of events in $WZ \to l\nu e^+e^-$ searches. Assuming equal $WW\gamma$ and WWZ couplings and a form factor scale of Λ = 2 TeV the following limits are obtained:

$$\begin{aligned} -0.25 < \Delta\kappa < 0.39 \quad (\lambda = 0) \\ -0.18 < \lambda < 0.19 \quad (\Delta\kappa = 0). \end{aligned} \tag{26}$$

The 95% C.L. 1-dimensional and 2-dimensional contour limits in other relations between $WW\gamma$ and WWZ coupling parameters are showed in Figure 32.

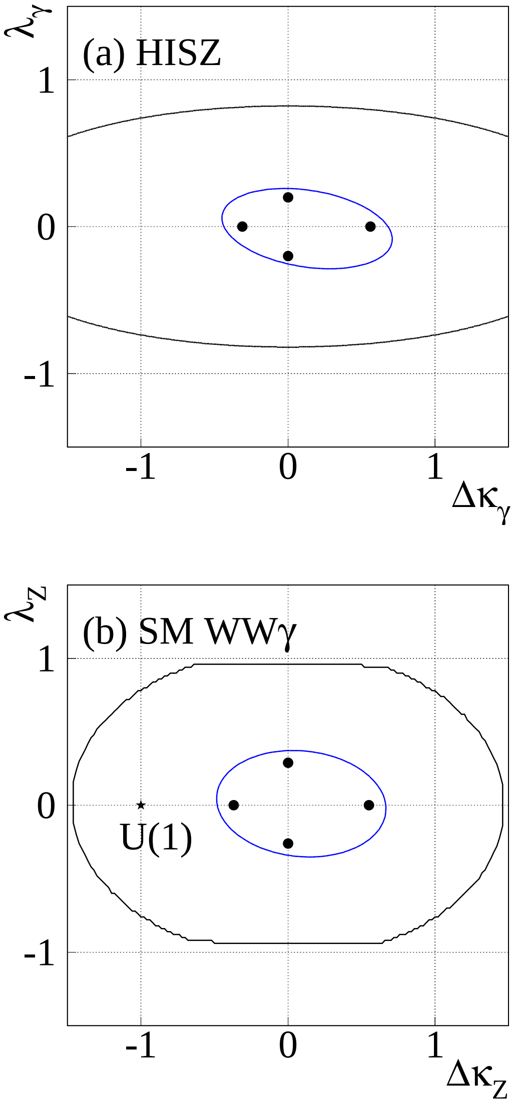

FIG. 32. Contour limits on anomalous couplings for Λ = 1.5 TeV and $\Delta g_1^Z = 0$ from the simultaneous fit to the DO data: (a) HISZ scenario; (b) assuming standard model value for $WW\gamma$ parameters. The solid circle are the 95% C.L. limits for 1-dimensional analysis. The inner and outer curves (where shown) are the 95% C.L. limits for the 2-dimensional and unitarity analyses, respectively.

VI. FUTURE PROSPECTS

The last decade has seen an impressive number of measurements of the W production and decay properties both from Run 1 at the Tevatron and the LEP II program. In the next ten years two proton machines, the Tevatron Collider at Fermilab and the Large Hadron Collider (LHC) at CERN are expected to collect even larger samples of W bosons. The former will start its $p\overline{p}$ Run 2 program in March 2001 with a stated goal of 2 fb^{-1} at $\sqrt{s} = 2$ TeV. The latter will gear up around 2005.

The main upgrades to the Tevatron are the addition of the Main Injector (MI) and the Recycler Ring (RR) (Montgomery, 1999). The MI is a proton synchrotron with a circumference half that of the Tevatron. It was designed to deliver high intensity $p\bar{p}$ beams to the Tevatron thus significantly enhancing the Tevatron luminosity. The RR is an 8 GeV permanent magnet ring equipped with stochastic cooling. Its main purpose is to store newly produced and unspent antiprotons between Tevatron runs, thus effectively doubling the number of $\bar{p}$ available for collisions. Both upgrades are presently being commissioned and a Tevatron engineering run with real collisions is expected in fall 2000.

Two sets of operating conditions are considered for the Run 2 of the Tevatron: 36 bunches crossing every 396 ns or 108 bunches crossing every 132 ns with typical delivered luminosities of 1 and 2×10^{32} cm^{-2} s^{-1}, respectively. The expected average number of overlapping interactions in a given beam crossing will be $\bar{N} = 3$ and $\bar{N} = 2$, respectively. This "classic" Run 2A scenario will be compared to a "stretched" Run 2, or Run 2B scenario (Amidei, 1996), with luminosities beyond 10^{32} cm^{-2} s^{-1} for $\int L = 10$ fb^{-1}. Both the CDF and DO Collaborations have extensively upgraded their detectors to fully exploit the discovery reach of the Tevatron in this new regime of "precision" hadron collider physics.

The CDF II detector (CDF Collaboration, 1996) will have a completely redesigned tracking system based on a seven-layer silicon inner tracker covering the azimuthal region $|\eta| < 2.0$ and an open cell drift chamber extending to $|\eta| < 1.0$, along with a new scintillator-based Time-of-Flight detector. Outside the solenoid, the original calorimeter and muon chambers surrounding the barrel region ($|\eta| < 1.0$) are complemented by a new plug calorimeter extending to $|\eta| < 3.6$ and an enhanced central and forward muon system able to provide almost full polar angle coverage for $|\eta| < 2.0$.

The DO Run 2 detector (DO Collaboration, 1996) will have a new inner silicon vertex detector surrounded by a new four-layer scintillating fiber tracker which together will ensure tracking coverage up to $|\eta| < 3.0$. These detectors are immersed in a 2 T magnetic field provided by a new superconducting solenoid. A new scintillator-based preshower detector is sandwiched between the solenoid and the original calorimeter cryostat to aid electron identification and triggering for $|\eta| < 2.5$. The existing central muon chambers will have a new faster readout. The forward muons will be identified with a new plastic Mini-Drift Tube detector with pixel readout covering the region $1.0 < |\eta| < 2.0$. The new Tevatron running conditions forced a complete redesign of the trigger and front-end electronics for CDF and DO.

The LHC will collide protons against protons every 25 ns at energies up to $\sqrt{s} = 14$ TeV with an initial "low" luminosity run at 10^{33} cm^{-2} s^{-1}, yielding $\int L = 10$ fb^{-1} per year, followed by a high luminosity run at 10^{34} cm^{-2} s^{-1} or higher, with $\int L = 100$ fb^{-1} per year. The latter configuration will see $\bar{N} \sim 20$ for a total of $\sim$ 2000 particles per crossing. Two general purpose experimental apparatus are being constructed, ATLAS (ATLAS Collaboration, 1994) and CMS (CMS Collaboration, 1994), which will probe the laws of fundamental interactions at effective energies of 1 TeV or higher. Both detectors emphasize muon spectroscopy as a safeguard against unexpected sources of background given the huge number of particles produced in each bunch crossing.

In the following we will report on the expectations for the Tevatron in the Main Injector era versus LEP II results and LHC sensitivities for W mass and width measurements, W charge asymmetry and QCD studies, rare decays and heavy charged bosons searches, and anomalous couplings. To set the scale of the discussion, table XIII gives the expected yield of W and diboson events at the Tevatron for CDF II assuming an integrated luminosity of 2 fb^{-1} and the Run 1B detector configuration. Also shown are the expected improvements in statistics coming from the increase in cross section and in acceptance.

A. W mass and width

The CDF/DO Run 1 combined measurement (see Figure 16) gives $M_W^{Tevatron} = 80.448 \pm 0.062$ GeV where the systematic error is dominated by uncertainties in the lepton energy deposition and track momentum response and resolution, and in the modelling of the recoil and W production. Uncertainties due to PDFs and QED radiative corrections amount to about 20 MeV and are common to all the Tevatron measurements. The LEP II average mass determination is $M_W^{LEP-II} = 80.401 \pm 0.048$ GeV (LEP WW Working Group, 2000). The projected LEP II precision is $\Delta M_W = 40$ MeV. The largest systematic uncertainty in the W mass measurement at LEP II is due to color reconnection effects.

The predicted W mass precision for each Tevatron experiment, with an integrated luminosity of 1(10) fb^{-1} is around 50(30) MeV per channel. In estimating the ΔM_W achievable at the Tevatron Run 2 one should distinguish between systematic errors from measurements that are obtained from control data samples, expected to decrease as $1/\sqrt{N}$, and systematic errors from theoretical sources. In the first group are uncertainties coming from the lepton and recoil energy/momentum scales and resolutions and backgrounds. In the second group are uncertainties coming from the W production and decay model, radiative corrections and PDFs. The "theoretical" uncertainties should be substantially reduced by the combination of new theoretical calculations and experimental results like the boson p_T measurements and the PDF constraints from W charge asymmetry measurements. A Tevatron Run 2A measurement with 25 MeV precision should be within reach.

It is worth noting that the presence of multiple interactions degrades the recoil energy determination, and therefore the W transverse mass resolution, by a factor proportional to $\sqrt{N}$. Thus the precision of the transverse mass fit does not improve as $1/\sqrt{N}$ when larger data samples are obtained by increasing the luminosity per bunch. The charged lepton p_T fit, which is much less sensitive to multiple interactions, will become the preferred technique at very high luminosity.

Within the SM, $\Delta M_W \sim 25$ MeV corresponds to $\Delta m_H/m_H \sim 40\%$, assuming all other inputs are precisely known. In this context, the current uncertainty of 5 GeV on the top quark mass is equivalent to $\Delta M_W \sim 30$ MeV. Thus it is important to improve the top mass precision also in Run 2. With an expected precision of 2.5 GeV, the top mass uncertainty will not limit the Higgs mass constraint. The running electromagnetic coupling constant $\alpha(M_Z)$ causes an uncertainty equivalent to $\Delta M_W \sim 15$ MeV, due to the uncertainty in the hadronic contribution to its evolution.

At present, the value of the Higgs mass that best fits all of the electroweak measurements performed by LEP, SLAC and Tevatron experiments is $m_H^{SM} = 67^{+60}_{-33}$ GeV[4] (LEP Collaborations, 2000a), i.e. m_H is currently constrained to within a factor of 2. After the Tevatron Run 2A, m_H should be constrained to within 50%.

The precise measurement of the W mass at the LHC presents some real challenges. Even at "low" luminosities, about 6×10^7 W events are expected per year making the statistical uncertainties completely negligible. The dominant systematic uncertainty, coming from the knowledge of the lepton energy scale, will limit the overall precision to 15 MeV with the assumption that the lepton energy and momentum scales can be understood at the 0.02% level.

The direct measurements of the W width from the tail of the m_T^W distribution, and its indirect extraction from the cross section ratio $R = \frac{\sigma_W \cdot B(W \to l\nu)}{\sigma_W \cdot B(Z \to l^+l^-)}$, provide an important SM consistency check. The Tevatron direct measurements of the W width is $\Gamma_W = 2.04 \pm 0.14$ GeV to be compared with the combined LEP II data of $\Gamma_W = 2.19 \pm 0.15$ GeV (LEP WW Working Group, 2000). With the statistics of the current Tevatron data samples, the indirect determination of the total W width from the partial leptonic cross sections (see Sec. V.C) is systematics-dominated and significantly more precise than the direct measurement from the high-m_T tail of the m_T distribution. However, the latter makes fewer model-dependent assumptions and is likely to improve more rapidly with higher statistics because the precision on Γ_W from R will be limited by the theoretical error on the σ_W/σ_Z production cross section ratio, currently around 1%. The projected Run 2 precision on the W width per experiment at the Tevatron, assuming integrated luminosities of 1(10) fb^{-1}, is 48(20) MeV from the W transverse mass fit in the $W \to e\nu$ channel alone. Combining the electron and muon channel for both experiments, a final overall precision of 10 MeV should be within reach.

[4] corresponding to $m_H < 188$ GeV at 95% C.L. Limits from direct searches at LEP yield $m_H > 107.9$ GeV at 95% C.L. (LEP Collaborations, 2000b).

B. W charge asymmetry and QCD studies

We saw in Sec. V.D how the measurement of the W charge asymmetry provides a very powerful tool for discriminating among different sets of PDFs at collider experiments. The sensitivity to the PDFs is greater in the region of $|\eta| > 2.0$. Therefore the improved rapidity coverage for tracking, calorimetry and muon detection in both CDF II and DO Upgrade will be very important for making the best use of the discriminating power of the W charge asymmetry. The precision of the measurements is expected to be statistically dominated for integrated luminosities up to 2 fb^{-1}.

The improved η coverage for jet reconstruction, together with the increased statistics available in Run 2, should also provide enough sensitivity to events with up to six jets produced in association with the W boson (see Fig. 25). As most of the inputs are determined from the data, we expect the p_T^W measurements to become more precise with larger data samples.

C. Rare W decays and heavy W' bosons

With the number of W decays produced with 10 fb^{-1}, one should be able to greatly improve the present Tevatron limits on $W \to \pi\gamma$ and $W \to D_s\gamma$ (see Sec. V.G) even though they will still be 2 orders of magnitude away from the branching ratios predicted by the SM. Their direct observation will also be out of reach at a high-luminosity LHC.

Helicity-independent searches for heavy charged boson decays $W' \to l\nu$ at the Tevatron yielded the best Run 1 limit of $M_{W'} > 720$ GeV at 95% C.L. assuming light, non-interacting, stable neutrinos and the suppression of the $W' \to WZ$ channel (see Sec. V.F.1). The limit is projected to improve to 990 GeV for a Run 2 integrated luminosity of 2 fb^{-1}. At LHC the sensitivity to a possible W' signal is predicted to extend out to masses of about 6 TeV.

D. Anomalous vector boson couplings

A DO simultaneous fit of the most sensitive distributions to anomalous WWV couplings has resulted in the 68% C.L. limits of $\lambda_\gamma = 0.00^{+0.10}_{-0.09}$ and $\Delta\kappa_\gamma = -0.08^{+0.34}_{-0.34}$ under the HISZ assumptions for $\Lambda = 2$ TeV. For comparison the current preliminary LEP II 1-D limits are $\lambda_\gamma = -0.016^{+0.026}_{-0.026}$ and $\Delta\kappa_\gamma = 0.021^{+0.063}_{-0.059}$ (LEP Electroweak TGC Working Group, 2000) and are expected to reach a precision level of 0.02 and 0.05 respectively, by the end of the LEP II program.

Since the sensitivity to anomalous production is limited by backgrounds, the cross sections (which depend on the square of the couplings) improve in precision as $1/\sqrt{N}$. For Run 2, the substantial increase in statistics should provide an improvement of order 2(5) over the present coupling limits for integrated luminosities of 1(10) fb^{-1}. At LHC, with 30 fb^{-1} of data, one expects a precision level of 0.003 for λ_γ and 0.04 for $\Delta\kappa_\gamma$.

The improved rapidity coverage for the Run 2 Tevatron detectors is also expected to improve the sensitivity to the amplitude zero effect in $p\overline{p} \to W\gamma$ production. Simulation studies indicate that with 1 fb^{-1} of data one should be able to establish the presence of a dip if both central and plug leptons can be used. It should be noted that the Tevatron might offer the only realistic chance of proving this SM prediction because the sensitivity to the amplitude zero effect at LHC is substantially reduced by large QCD corrections.

VII. CONCLUSIONS

The production of high-statistics W samples at the Tevatron has resulted in precision measurements of its properties. The current world average of the direct measurements of the W mass is $M_W = 80.419 \pm 0.038$ GeV/c^2, corresponding to a precision of 0.05%. The measurements of the W width, the production cross section and the event kinematics are consistent with the SM prediction. A precise measurement of the W charge asymmetry has provided an additional handle on reducing the W mass uncertainty as well as challenging the theory to devise a more accurate description of the data with new sets of parton distribution functions. New limits have been set for the branching ratio into rare decay modes and the masses of a heavy W' and right-handed W boson. Studies of the trilinear gauge boson couplings have shown that the production of $W\gamma$, WW and WZ events is in agreement with the prediction of the SM, within the experimental sensitivity.

The upgraded Tevatron and the DO and CDF detectors will begin running in the year 2001, followed by the operation of the LHC together with the ATLAS and CMS detectors within this decade. Improvements in the precision measurements of the W properties, coupled with the improved measurement of the top quark mass, will yield predictions for the Higgs mass and provide crucial tests of the self-consistency of the SM.

ACKNOWLEDGMENTS

We wish to thank our CDF and DO colleagues for producing such fruitful results over last decade. We also wish to express our thanks to F. Bedeschi, M. Campbell, and A. Goshaw for encouraging us to write this review. We thank W. Ashmanskas, J. Dittman, J. Ellison, C. Gerber, Y. Kim, and W. Robertson for their assistance with the figures.

REFERENCES

Abachi, S. et al., 1994, Nucl. Inst. Meth. **A338**, 185
Abachi, S. et al., 1995, Phys. Lett. **358B**, 405
Abachi, S. et al., 1995, Phys. Rev. Lett. **75**, 1023
Abachi, S. et al., 1995, Phys. Rev. Lett. **75**, 1456
Abachi, S. et al., 1995, Phys. Rev. Lett. **75**, 3226
Abachi, S. et al., 1996, Phys. Rev. Lett. **76**, 3271
Abachi, S. et al., 1996, Phys. Rev. Lett. **77**, 3309
Abachi, S. et al., 1997, Phys. Rev. Lett. **78**, 3634
Abachi, S. et al., 1997, Phys. Rev. Lett. **79**, 1441
Abbott, B. et al., 1998, Phys. Rev. **D58** , 12002
Abbott, B. et al., 1998, Phys. Rev. **D58**, Rapid Comm. , 51101
Abbott, B. et al., 1998, Phys. Rev. Lett. **80**, 2063
Abbott, B. et al., 1998, Phys. Rev. Lett. **80**, 3008
Abbott, B. et al., 1999, Phys. Rev. **D60** , 52003
Abbott, B. et al., 1999, Phys. Rev. **D60** , 72002
Abbott, B. et al., 2000, Phys. Rev. **D61** , 32004
Abbott, B. et al., 2000, Phys. Rev. **D61** , 72001
Abbott, B. et al., 2000, Phys. Rev. Lett. **84**, 222
Abbott, B. et al., 2000, Phys. Rev. Lett. **84**, 2792
Abbott, B. et al., 2000, Phys. Rev. Lett. **84**, 5710
Abe, F. et al., 1988, Nucl. Inst. Meth. **A271**, 387
Abe, F. et al., 1989, Phys. Rev. Lett. **62**, 1005
Abe, F. et al., 1990, Phys. Rev. **D41**, 2330
Abe, F. et al., 1990, Phys. Rev. Lett. **65**, 2243
Abe, F. et al., 1991, Phys. Rev. **D43**, 2070
Abe, F. et al., 1991, Phys. Rev. Lett. **66**, 2951
Abe, F. et al., 1991, Phys. Rev. Lett. **67**, 2609
Abe, F. et al., 1992, Phys. Rev. Lett. **68**, 1458
Abe, F. et al., 1992, Phys. Rev. Lett. **69**, 2160
Abe, F. et al., 1994, Phys. Rev. Lett. **73**, 2296
Abe, F. et al., 1995, Phys. Rev. Lett. **74**, 341
Abe, F. et al., 1995, Phys. Rev. Lett. **74**, 850
Abe, F. et al., 1995, Phys. Rev. Lett. **74**, 1936
Abe, F. et al., 1995, Phys. Rev. Lett. **74**, 2900
Abe, F. et al., 1995, Phys. Rev. Lett. **75**, 11; Phys. Rev. **D52**, 4784
Abe, F. et al., 1995, Phys. Rev. Lett. **75**, 1017
Abe, F. et al., 1995, Phys. Rev. **D52**, 2624
Abe, F. et al., 1996, Phys. Rev. Lett. **76**, 2852

Abe, F. et al., 1996, Phys. Rev. Lett. **76**, 3070
Abe, F. et al., 1997, Phys. Rev. Lett. **78**, 4536
Abe, F. et al., 1997, Phys. Rev. Lett. **79**, 4760
Abe, F. et al., 1998, Phys. Rev. **D58**, 31101
Abe, F. et al., 1998, Phys. Rev. **D58**, 91101
Abe, F. et al., 1998, Phys. Rev. Lett. **81**, 5754
Abe, F. et al., 1999, Phys. Rev. Lett. **82**, 271; Phys. Rev. Lett. **82**, 2808
Abe, F. et al., 1999, Phys. Rev. **D59**, 52002
Abe, F. et al., 1999, FERMILAB-PUB-99/249-E
Affolder, T. et al., 2000, Phys. Rev. Lett. **84**, 845
Affolder, T. et al., 2000, submitted to Phys. Rev. Lett.
Albajar, C. et al., 1989, Z. Phys. **C44**, 15
Albajar, C. et al., 1990, Phys. Lett. **B241**, 283
Alitti, J. et al., 1990, Phys. Lett. **241B**, 150
Alitti, J. et al., 1991, Z. Phys. **C49**, 17
Alitti, J. et al., 1992, Phys. Lett. **276B**, 354
Alitti, J. et al., 1992, Phys. Lett. **276B**, 365
Alitti, J. et al., 1992, Phys. Lett. **277B**, 203
Alitti, J. et al., 1993, Nucl. Phys. **B400**, 3
Amidei, D. et al., 1996, FNAL-Pub-96/082, "Report of the Tev-2000 Study Group"
Ansari, R. et al., 1987, Phys. Lett. **186B**, 440
Ansari, R. et al., 1987, Phys. Lett. **186B**, 452
Ansari, R. et al., 1987, Phys. Lett. **195B**, 613
Appel, J. et al., 1986, Z. Phys. **C30**, 1
Arnellos, L., W. Marciano, and Z. Parsa, 1982, Nucl. Phys. **B196**, 378
Arneodo, M. et al., 1997, Nucl. Phys. **B487**, 3
Arnison, G. et al., 1983, Phys. Lett. **122B**, 103
Arnison, G. et al., 1983, Phys. Lett. **126B**, 398
Arnison, G. et al., 1985, Nuovo Cimento. **V44**, 1
Arnison, G. et al., 1986, Phys. Lett. **166B**, 484
Arnold, P. and M. Reno, 1989, Nucl. Phys. **B319**, 37
ATLAS Collaboration, 1994, CERN/LHCC/94-43, "ATLAS Technical Proposal"
Bagnaia, P. et al., 1983, Phys. Lett. **129B**, 130
Balazs, C. and C. Yuan, 1997, Phys. Rev. **D56**, 5558
Banner, M. et al., 1983, Phys. Lett. **122B**, 476
Barberio, E. and Z. Was, 1994, Comp. Phys. Commun. **79**, 291
Barbieri, R. et al., 1989, Phys. Rev. **D39** 1229
Baur, U. and E. Berger, 1990, Phys. Rev. **D41**, 1476
Baur U., T. Han and J. Ohnemus, 1993, Phys. Rev. **D48** 5140
Baur U., T. Han and J. Ohnemus, 1995, Phys. Rev. **D51** 3381
Baur U., T. Han and J. Ohnemus, 1996, Phys. Rev. **D53** 1098
Baur, U., S. Keller and D. Wackeroth, 1999, Phys. Rev. **D59**, 13002
Benjamin, D., 1996, AIP Conference Proceedings **357**, 370
Berends, F. and R. Kleiss, 1985, Z. Phys. **C27**, 365
Berends, F. et al., 1991, Nucl. Phys. **B357**, 32
Berger, E. et al., 1989, Phys. Rev. **D40**, 83, *erraum-ibid*, **D40**, 3789
Brun, R. et al., 1978, CERN-DD-78-2-Rev
CDF Collaboration, 1996, FNAL-Pub-96/390-E, "CDF II Detector Technical Design Report"
CMS Collaboration, 1994, CERN/LHCC/94-38, " CMS Technical Proposal"
Chankowski, P. et al., 1994, Nucl. Phys. **B417**, 101
Collins J., D. Soper, 1981, Nucl. Phys. **B193**, 381
Collins J., D. Soper and G. Sterman, 1985, Nucl. Phys. **B250**, 199
D0 Collaboration, 1996, FNAL-Pub-96/357-E, "The D0 Upgrade - The Detector and Its Physics"
Dabelstein, A., W. Hollik, and W. Mosle, 1995, " Perspective for Electroweak Interactions in e^+e^- Collisions", ed. by B. Kniehl, 345
Degrassi, G., P. Gambino, and A. Sirlin, 1997, Phys. Lett. **B394**, 188
Degrassi, G. et al., 1998, Phys. Lett. **B418**, 209
Drell, S, and T. Yan, 1970, Phys. Rev. **25**, 316
Ellis, R, and S. Veseli, 1998, Nucl. Phys. **B511**, 649
Ellison, J, and J. Wudka, 1998, Ann. Rev. Nucl. Part. Sci., **48**, 33
Garcia D, and J. Sola, 1994, Mod. Phys. Lett. **A9**, 211
Giele, W., E. Glover, and D. Kosower, 1993, Nucl. Phys. **B403**, 633
Giele, W., S. Keller, 1998, Phys. Rev. **D57**, 4433
Glashow, S., 1961, Nucl. Phys. **22**, 579
Grünewald, M., 1999, Phys. Rep. **322**, 125
Hagiwara, K. et al., 1993, Phys. Rev. **D48**, 2182
Hasert, F. et al., 1973, Phys. Lett **46B**, 138
LEP Collaborations, LEP Electroweak Working Group, and SLD Heavy Flavour and Electroweak Group, 2000, CERN-EP-2000-016
LEP Collaborations, LEP Working Group for Higgs boson searches, 2000 CERN-EP-2000-055
LEP Electroweak TGC Working Group, 2000, LEPEWWG/TGC/2000-01
LEP WW Working Group, 2000, LEPEWWG/WW/00-01
Ladinsky, G. and C. Yuan, 1994, Phys. Rev. **D50**, 4239
Lai, H., 1995, Phys. Rev. **D51**, 4763
Lai, H., 1997, Phys. Rev. **D55**, 1280
Langacker, P., 1989, Phys. Rev. **D40**, 1229
Llewellyn Smith, C., and J. Wheater, 1981, Phys. Lett. **B105** 486
Marchesini, G. and B. Webber, 1988, Nucl. Phys. **B310**, 461
Marciano, W. and A. Sirlin, 1980, Phys. Rev. **D22**, 2695
Martin, A. et al., 1989, Mod. Phys. Lett. **A4**, 1135
Martin, A. et al., 1993, Phys. Lett. **306B**, 145
Martin, A. et al., 1996, Phys. Lett. **387B**, 419
Martin, A. et al., 1998, Eur. Phys. J. **C4**, 463
Mirkes, E., S. Willfahrt and D. Zeppenfeld, 1997, Jerusalem, High Energy Physics Conference Proceedings, 499
Mohapatra, R., 1992, "Unification and Supersymmetry", (Springer-Verlag, New York)
Montgomery, H., 1999, FERMILAB-CONF-99-057, "Physics with the Main Injector"
Nodulman, L., 1996, Int. Conf. High Energy Phys. 28th, Warsaw, Poland
Ohnemus, J., 1991, Phys. Rev. **D44**, 1403
Ohnemus, J., 1991, Phys. Rev. **D44**, 3477
Ohnemus, J., 1993, Phys. Rev. **D47**, 940
Ohnemus, J., and W. Stirling, 1993, Phys. Lett. **B298** 230
Olive, K. et al., 1981, Nucl. Phys. **B180**, 497
Paige, F. and S. Protopopescu, 1986, BNL Report, BNL38034
Particle Data Group, 1994, Phys. Rev. **D50**, Sec 17.5.3.2
Particle Data Group, 1998, Review of Particle Physics
Pierce, D. et al., 1997, Nucl. Phys. **B491**, 3
Raffaelt, G. et al., 1988, Phys. Rev. Lett **60**, 1793

Ramond, P., 1983, Ann. Rev. Nucl. Part. Sci., **33**, 31
Salam, A., 1969, “Elementary Particle Theory”, ed. N. Svartholm (Almquist and Wiksells, Stockholm), 467
Sirlin, A., 1980, Phys. Rev. **D22**, 971
Sjostrand, T., 1985, Phys. Lett. **157B**, 321
Sjostrand, T. and M. van Zijl, 1987, Phys. Rev. **D36**, 2019
Weinberg, S, 1967, Phys. Lett. **19**, 1264
Yang, U., A. Bodek, and Q. Fan, 1998, The Proceedings of the QCD Moriond Conference

TABLE I. CDF and DO electron and muon channel W mass results and statistical errors (in GeV) from Run 1B.

CDF	central electron	central muon
m_T	80.473 ± 0.065	80.465 ± 0.100
DO	central electron	forward electron
m_T	80.438 ± 0.070	80.757 ± 0.107
$p_T(e)$	80.475 ± 0.087	80.547 ± 0.128
$p_T(\nu)$	80.37 ± 0.11	80.740 ± 0.159

TABLE II. Systematic uncertainties in the W mass (in MeV) in the CDF measurements from the Run 1A data.

Source	$W \to e\nu$	$W \to \mu\nu$	common
lepton scale	75	85	
lepton resolution	25	20	
pdfs	15	15	15
p_T^W	15	20	3
recoil	37	35	
higher order QED	20	10	5
trigger, lepton identification bias	-	15 ⊕ 10	
backgrounds	5	25	
total	92	103	16

TABLE III. W mass uncertainties (in MeV) in the combined DO measurement from the Run 1B data.

Source	Uncertainty in MeV
W statistics	61
Z statistics	59
calorimeter linearity	25
calorimeter uniformity	8
electron resolution	19
electron angle calibration	10
recoil response	25
recoil resolution	25
electron removal	12
selection bias	3
backgrounds	9
pdf	7
parton luminosity	4
$p_T(W)$	15
$\Gamma(W)$	10
radiative corrections	12

TABLE IV. Uncertainties in the CDF W width Γ_W measurements (in MeV) from the 1994-1995 data.

Source	$W \to e\nu$	$W \to \mu\nu$	common
statistics	125	195	
lepton E or p_T non-linearity	60	5	
recoil model	60	90	
p_T^W	55	70	
backgrounds	30	50	
detector modelling, lepton ID	30	40	
lepton E or p_T scale	20	15	
lepton resolution	10	20	
pdfs	15	15	15
M_W	10	10	10
higher order QED	10	10	10
total systematic	115	135	25
total statistical ⊕ systematic	170	235	25

TABLE V. DO and CDF number of events N_{evts}, background fractions f, kinematical plus geometrical acceptance A, trigger plus selection efficiency ϵ and total cross section times leptonic branching fraction $\sigma \cdot B$ for W and Z reconstructed in both leptonic channels. The standard model predictions are (see reference Abbott (1999a) for a discussion) $\sigma_W \cdot B(W \to l\nu) = 2.42^{+0.13}_{-0.11}$ nb and $\sigma_Z \cdot B(Z \to l^+l^-) = 0.226^{+0.011}_{-0.009}$ nb.

DO	$W \to e\nu$	$Z \to ee$	$W \to \mu\nu$	$Z \to \mu\mu$
N_{evts}	67078	5397	1665	77
f (%)	6.4±1.4	4.5±0.5	22.1±1.9	10.1±3.7
A (%)	46.5±0.4	36.6±0.3	24.8±0.7	6.5±0.4
ϵ (%)	67.1±0.9	74.4±1.1	21.9±2.2	52.7±4.9
$\sigma \cdot B$ (nb)	2.31±0.11	0.221±0.011	2.09±0.25	0.178±0.032
L(pb^{-1})	84.5±3.6	84.5±3.6	11.4±0.6	11.4±0.6
CDF	$W \to e\nu$	$Z \to ee$	$W \to \mu\nu$	$Z \to \mu\mu$
N_{evts}	13796	1312	1436	2417
f (%)	12.3±1.2	2.1±0.7	15.3±2.1	7.5±1.6
A (%)	34.2±0.8	40.9±0.5	19.0±0.9	16.6±0.4
ϵ (%)	72.0±1.3	69.6±1.7	82.1±3.5	58.1±1.3
$\sigma \cdot B$ (nb)	2.49±0.12	0.229±0.012	2.21±0.22	0.233±0.018
$L(pb^{-1})$	19.7±0.7	19.7±0.7	3.54±0.24	107.4±7.1

TABLE VI. Results and uncertainties in the DO R measurement from Run 1B, and the CDF R measurement from Run 1A.

	DO	CDF
R	10.43±0.27	10.90±0.32(stat)±0.29(syst)
ratio of events	12.43±0.18	
efficiency ratio	1.108±0.007	1.035±0.016
acceptance ratio	0.787±0.007	0.835±0.013
NLO electroweak	1.00±0.01	

TABLE VII. Inputs used by CDF and DO to extract Γ_W from $R = \frac{\sigma_W \cdot B(W \to e\nu)}{\sigma_Z \cdot B(Z \to e^+e^-)}$.

	CDF	DO
σ_W/σ_Z	3.35±0.03	3.362±0.053
$\Gamma(Z)$	2.4969±0.0038 GeV	
$\Gamma(Z \to e^+e^-)$	83.98±0.18 MeV	
$B(Z \to e^+e^-)$		0.03367±0.00006
$\Gamma(W \to e\nu)$	225.9±0.9 MeV	227.0±1.1 MeV

TABLE VIII. Backgrounds(%) in the $W \to e\nu$ and $W \to \mu\nu$ charge asymmetry data samples. Note: There is also a 4% background from low momentum muons reconstructed as high momentum muons in the Forward μ data.

Sample	$W \to \tau\nu$	QCD dijets	$Z \to l^+l^-$
Central e	2.0 ± 0.2	0.7 ± 0.2	< 0.2
Central μ	2.0 ± 0.2	0.6 ± 0.2	4.7 ± 0.7
Plug-SVX e	2.0 ± 0.2	1.6 ± 0.3	< 0.2
Plug-CTC e	2.0 ± 0.2	2.4 ± 0.6	< 0.2
Forward μ (See note)	2.0 ± 0.2	4 ± 2	6.5 ± 0.6

TABLE IX. Summary of CDF and DO $W' \to l\nu$ searches. The DO search in the $(M_{W'}, M_\nu)$ plane (see Sec. V.F.2) yields the limit $M_{W'}(95\%CL) > 720$ GeV for a light ν.

	CDF	CDF	DO
	$W' \to \mu\nu$	$W' \to e\nu$	$W' \to e\nu$
N_{obs}	31992	10534	9135
$L(\mathrm{pb}^{-1})$	107	19.7	13.9
N_{obs} ($m_T > 150$ GeV)			16
N'_{bkg} ($m_T > 150$ GeV)			19.7±5.7
N_{obs} ($m_T > 200$ GeV)	14	5	
N'_{bkg} ($m_T > 200$ GeV)	11.8±0.9	7	
$M_{W'}(95\%CL)$ limit	660 GeV	652 GeV	610 GeV

TABLE X. Summary of DO and CDF analysis for $W\gamma \to l\nu\gamma$.

	DO		CDF	
	$e\nu\gamma$	$\mu\nu\gamma$	$e\nu\gamma$	$\mu\nu\gamma$
N_{obs}	57	70	75	34
N_{bkg}	15.2±2.5	27.7±4.7	16.1±3.5	10.3±1.6
N_{sgn}	41.8±8.2	42.3±9.0	58.9±9.4	10.3±6.0
N_{SM}	43.6±3.1	38.2±2.8	53.5±6.8	21.8±4.3
$E_T^{min}(\gamma)$	10 GeV		7 GeV	
$\sigma \times B(W \to l\nu)_{expt}$	11.3±2.2 pb		20.7±3.0 pb	
$\sigma \times B(W \to l\nu)_{SM}$	12.5±1.0 pb		18.6±2.8 pb	
L	92.8 pb^{-1}		67 pb^{-1}	

TABLE XI. Summary of DO analysis for $WW/WZ \to l\nu jj$, $l = e$ or μ.

	$e\nu jj$	$\mu\nu jj$
Backgrounds		
$W+ \geq$ 2jets	341.7±38.3	105±19
QCD multijets	116.5±12.6	117±24
$t\bar{t} \to l\nu\ jj$	4.6± 1.3	2.7±1.2
N_{obs}	483	224
N_{bkg}	462.8±40.3	224±31
N_{SM}	20.7±3.1	4.5±0.8

TABLE XII. Summary of DO analysis for $WZ \to l\nu ee$, $l = e$ or μ

	$e\nu ee$	$\mu\nu ee$
N_{obs}	1	0
N_{bkg}	0.38±0.14	0.12±0.04
N_{SM}	0.1±0.01	0.10±0.01

TABLE XIII. Expected W event yields for CDF II with 2 fb^{-1} of data: events when Run Ib detector configuration is assumed (II column), improvement factors when increase in cross-section (III column) and increased acceptance (last column) are taken into account. For $W\gamma$ the cuts assumed are $E_T^\gamma > 10$ GeV, $|\eta^\gamma| < 1$.

Channel	Events	$\sigma_{2.0\ TeV}/\sigma_{1.8\ TeV}$	$A_{\lvert\eta\rvert<2.0}/A_{\lvert\eta\rvert<1.0}$
$W \to e\nu$	1.4×10^6	1.12	2.0
$W \to \mu\nu$	6.5×10^5	1.12	2.6
$W\gamma$	1.5×10^3	1.13	1.5
$WW \to l\nu l\nu$	77	1.17	2.1
$WZ \to l\nu ll$	10	1.22	4.4